

# A comparative study of self-propelled and towed wakes in a stratified fluid

KYLE A. BRUCKER AND SUTANU SARKAR†

Department of Mechanical and Aerospace Engineering, University of California,  
San Diego, CA 92093, USA

(Received 8 May 2009; revised 2 January 2010; accepted 3 January 2010;  
first published online 12 April 2010)

Direct numerical simulations (DNS) of axisymmetric wakes with canonical towed and self-propelled velocity profiles are performed at  $Re = 50\,000$  on a grid with approximately 2 billion grid points. The present study focuses on a comparison between towed and self-propelled wakes and on the elucidation of buoyancy effects. The development of the wake is characterized by the evolution of maxima, area integrals and spatial distributions of mean and turbulence statistics. Transport equations for mean and turbulent energies are utilized to help understand the observations. The mean velocity in the self-propelled wake decays more rapidly than the towed case due to higher shear and consequently a faster rate of energy transfer to turbulence. Buoyancy allows a wake to survive longer in a stratified fluid by reducing the  $\langle u'_1 u'_3 \rangle$  correlation responsible for the mean-to-turbulence energy transfer in the vertical direction. This buoyancy effect is especially important in the self-propelled case because it allows regions of positive and negative momentum to become decoupled in the vertical direction and decay with different rates. The vertical wake thickness is found to be larger in self-propelled wakes. The role of internal waves in the energetics is determined and it is found that, later in the evolution, they can become a dominant term in the balance of turbulent kinetic energy. The non-equilibrium stage, known to exist for towed wakes, is also shown to exist for self-propelled wakes. Both the towed and self-propelled wakes, at  $Re = 50\,000$ , are found to exhibit a time span when, although the turbulence is strongly stratified as indicated by small Froude number, the turbulent dissipation rate decays according to inertial scaling.

---

## 1. Introduction

Historically, the study of turbulent wakes in stratified fluids did not involve spheres, instead slender bodies, either towed or propelled via their own thrust were used. A comprehensive review of these early studies is given in Lin & Pao (1979). In brief, these early studies found that a stratified wake is qualitatively different from its unstratified counterpart: vertical growth and entrainment are suppressed, propagating internal waves that can transport momentum and energy away from the wake are present and coherent late time vortices are enabled. After these early experiments the focus shifted to the study of turbulent wakes of towed spheres in stable linear background density gradients. Experiments and numerical simulations of this flow provided great insight into the fundamental problem of spatially limited turbulent patches in the

† Email address for correspondence: ssarkar@ucsd.edu

atmosphere and ocean, as well as the practical problem of turbulent wakes generated by propelled slender bodies. A comprehensive review of the results of these towed sphere studies is given in Spedding (2002). Of particular interest is the identification of a non-equilibrium phase (NEQ) in which the flow transitions from a near-wake (NW) region comprised of a three-dimensional turbulent flow with negligible buoyancy effects to a quasi-two-dimensional-phase (Q2D) where the flow is constrained by a vertical density gradient. Spedding (1997) argues that presence of this NEQ stage is a general characteristic of all spatially limited patches of decaying turbulence. Spedding (2001) notes that the NEQ phase is the least understood, in part due to the difficulties in experimental and theoretical analysis that arise from the complex coupling between anisotropic vertical motion and buoyancy forces. The potential universality of the NEQ phase requires assessment with studies in which the velocity profile is not that of a towed sphere and where the Reynolds number is high.

Recently, the focus of stratified wake research has shifted to self-propelled bodies. The recent study of Meunier & Spedding (2006) considers the wake of a bluff body in three configurations: momentum excess, zero momentum and zero momentum with a slight angle of attack focusing mainly on the coherent structures in the late wake. In the experiments, the body was towed at a certain speed and the drag measured; this measurement was then used in a subsequent run where thrust equal to the measured drag was added. The conditions under which they could achieve a self-propelled wake required less than a  $\pm 2\%$  difference between thrust and drag. If this condition was not met, a thrust/drag wake ensued which dominated the self-propelled portion of the wake. Achieving this balance proved extremely difficult and they called into question whether a truly momentumless wake could exist in the field. Meunier & Spedding (2006) found that the turbulent fluctuations in the far wake were an order of magnitude larger than the mean velocity in the zero-net-momentum self-propelled case, actually terming the mean velocity profile a ‘null’ profile. Voropayev *et al.* (1999) and Voropayev & Fernando (2009) studied, experimentally, the wake of a maneuvering body and found that the addition of a small amount of impulsive momentum to a self-propelled body in steady motion results in coherent vortices in the far wake.

In conjunction with the recent shift to wakes of propelled/maneuvering slender bodies, there has been an interest in wakes at high  $Re$ . The high-resolution numerical simulations of towed wakes by Diamessis & Spedding (2006) found that previous high- $Re$  large eddy simulations (LES) of Dommermuth *et al.* (2002) captured the large-scale features of the flow, but may not have captured important small-scale physics such as the formation of secondary Kelvin–Helmholtz type instabilities in the late wake which were driven by intensified vertical shear. For the canonical towed wake, Diamessis & Spedding (2006) also observed that the length of the NEQ phase was extended at high  $Re$ , a result not observed in the LES of Dommermuth *et al.* (2002).

If the NEQ phase is universal to all patches of stratified turbulence, or even all stratified wakes, it should be discernible in wakes that do not have a velocity profile corresponding to a towed sphere. Here, direct numerical simulations (DNS) at a relatively high Reynolds number,  $Re \equiv UD/\nu = 50\,000$ , where  $U$  is relative velocity of the flow past the body,  $D$  is the diameter of the body and  $\nu$  is the kinematic viscosity of the fluid, are utilized to compare the evolution of a towed wake profile to a velocity profile that is multiply inflected and has no initial net momentum.

The present study will help resolve the following unanswered questions regarding stratified wakes: Are the various stages of evolution observed in towed wakes in stratified fluids observed in the zero initial net-momentum wake? How is the evolution

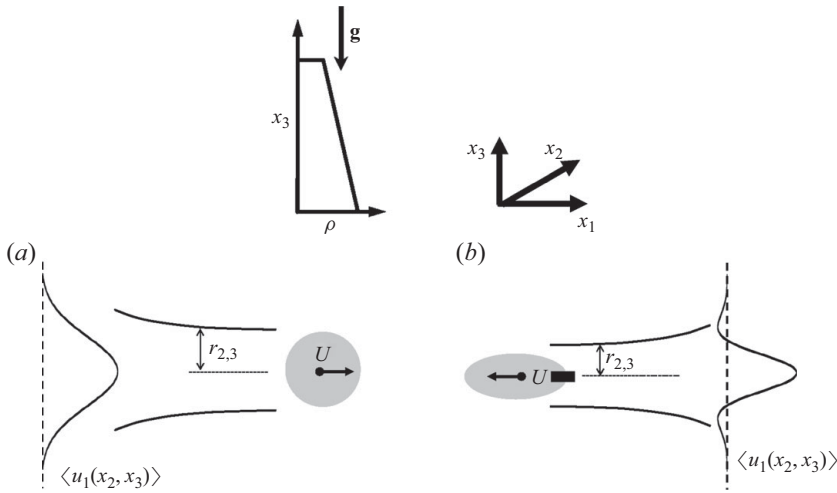


FIGURE 1. Schematic of wake flows: (a) towed, (b) self-propelled. Profiles of the mean velocity  $\langle u_1 \rangle$  in the laboratory frame show a qualitative difference between the towed and self-propelled case,  $\mathbf{g} = [0, 0, -g]$ .

of wake kinetic energy and its spatial distribution affected by the presence of initial net momentum? Lastly, the present stratified wake simulations are used to address fundamental questions regarding high- $Re$  turbulence subject to stratification.

The paper is organized as follows: § 2 discusses the computational model employed and the numerical techniques used to simulate stratified wakes at high  $Re$ . Section 3 provides an overview of the tools used to analyse the DNS data. Section 4 introduces the results using visualizations. Section 5 discusses the towed wake results with an emphasis on comparisons to existing experiments and simulations. Section 6 begins the analysis of self-propelled wake simulations by comparing their characteristic velocity and length scales to those of the towed wake. Section 7 continues this comparison in terms of evolution of mean kinetic energy (*m.k.e.*) and turbulent kinetic energy (*t.k.e.*). Section 8 discusses the terms in the *t.k.e.* budget, turbulence components and the turbulent dissipation rate including its inertial scaling and anisotropy. The major results of the study are summarized in § 9.

## 2. Formulation

A laboratory wake is typically produced by towing a body, say with velocity  $U$ , and the fluid behind the body has a velocity profile in the laboratory frame as shown in figure 1(a). In a frame moving with the body, the velocity profile corresponds to a defect velocity with respect to the external free stream of speed  $U$ , and the resultant wake is called a towed wake. Also of relevance to submersible applications is the wake of a body that moves under its own power so that thrust and drag are present resulting in a self-propelled wake, with typical velocity of the fluid behind it as shown in figure 1(b). The qualitatively different shape (multiply inflected profile) of the self-propelled wake velocity profile with respect to the towed case is worth noting, as a special case the self-propelled profile can have zero net momentum. The wake shown in figure 1(b) models a jet-driven body, and the effects of swirling motions from propellers, sail planes and other control surfaces are not considered. In a stratified fluid, the initial flow around the body would cause lee wave drag and

an exactly momentumless velocity profile would be a slightly overthrust version of figure 1(b). Based on the results of Lofquist & Purtell (1984), the change in the drag coefficient at  $Fr = 4$  is about 2%. In the remainder of the paper, the terms self-propelled and momentumless are taken to mean an initially momentumless wake neglecting lee wave drag.

### 2.1. Model

In the computational model, the flow behind the body is simulated in the laboratory frame. A temporal flow approximation is employed and the distance from the body,  $X$  in the laboratory frame, is equivalent to  $Ut$  in the simulation. Such a temporal approximation has been adopted with success in previous axisymmetric wake simulations in both unstratified and stratified fluids (Gourlay *et al.* 2001; Dommermuth *et al.* 2002; Diamessis, Domaradzki & Hesthaven 2005), plane wake simulations in unstratified fluids (Ghosal & Rogers 1997; Moser, Rogers & Ewing 1998) and other free shear flows in stratified (Brucker & Sarkar 2007; Basak 2005; Pham, Sarkar & Brucker, 2009) and unstratified fluids (Rogers & Moser 1994). The three-dimensional, unsteady Navier–Stokes equations are numerically solved directly and without any turbulence model. The density  $\rho^*$  is a function of the vertical coordinate  $x_3$  and gravity  $g$  acts in the  $-x_3$  direction.

### 2.2. Governing equations

The conservation equations for continuity, momentum and density for an unsteady (here a superscript  $*$  denotes a dimensional quantity) incompressible flow are

continuity:

$$\frac{\partial u_k^*}{\partial x_k^*} = 0, \quad (2.1)$$

momentum:

$$\frac{\partial u_i^*}{\partial t^*} + \frac{\partial (u_k^* u_i^*)}{\partial x_k^*} = -\frac{1}{\rho_0} \frac{\partial \tilde{p}^*}{\partial x_i^*} + \nu \frac{\partial^2 u_i^*}{\partial x_k^* \partial x_k^*} - \frac{\tilde{\rho}^*}{\rho_0} g \delta_{i3}, \quad (2.2)$$

density:

$$\frac{\partial \rho^*}{\partial t^*} + \frac{\partial (u_k^* \rho^*)}{\partial x_k^*} = \kappa \frac{\partial^2 \rho^*}{\partial x_k^* \partial x_k^*}. \quad (2.3)$$

The Boussinesq approximation has been employed so that variations in density are ignored except where they give rise to a gravitational force. The density is decomposed as a constant reference density plus a small departure which is further split into a mean and fluctuation:

$$\rho^* = \rho_0 + \bar{\rho}^*(x_3, t) + \tilde{\rho}^*(x_i, t). \quad (2.4)$$

Here,  $\bar{\rho}^*(x_3, t)$  is obtained by averaging over the  $x_1$  and  $x_2$  directions, and  $\tilde{\rho}^*$  denotes deviations with respect to the hydrostatic pressure associated with  $\bar{\rho}^*(x_3, t)$ .

Equations (2.1)–(2.3) are non-dimensionalized with the relative body velocity  $U$ , the characteristic density  $\rho_0$ , the dimensional density gradient  $C^* = |d\bar{\rho}^*/dx_3^*|(t=0)$ , and twice the initial wake radius,  $D \equiv 2r_0$ . With the introduction of these scales, new non-dimensional variables are obtained as

$$t = \frac{t^* U}{D}, \quad x_i = \frac{x_i^*}{D}, \quad u_i = \frac{u_i^*}{U}, \quad \rho = \frac{\rho^*}{\rho_0}, \quad \tilde{\rho} = \frac{\tilde{\rho}^*}{DC^*}, \quad p = \frac{\tilde{p}^*}{\rho_0 U^2}. \quad (2.5)$$

After substitution and simplification, the non-dimensional equations are continuity:

$$\frac{\partial u_k}{\partial x_k} = 0, \quad (2.6)$$

momentum:

$$\frac{\partial u_i}{\partial t} + \frac{\partial (u_k u_i)}{\partial x_k} = -\frac{\partial p}{\partial x_i} + \frac{1}{Re} \frac{\partial^2 u_i}{\partial x_k \partial x_k} - \frac{1}{Fr^2} \tilde{\rho} \delta_{i3}, \quad (2.7)$$

density:

$$\frac{\partial \rho}{\partial t} + \frac{\partial (u_k \rho)}{\partial x_k} = \frac{1}{Re Pr} \frac{\partial^2 \rho}{\partial x_k \partial x_k}, \quad (2.8)$$

where the relevant non-dimensional parameters are as follows: the Reynolds number,  $Re = UD/\nu$ , the Prandtl number,  $Pr = \nu/\kappa$ , and the internal Froude number,  $Fr = U/(N^* D)$  where  $N^*$  is the Brunt–Väisälä frequency defined by  $N^* = [-gC^*/\rho_0]^{1/2}$ . The non-dimensional buoyancy frequency is  $N \equiv Fr^{-1}$ . In the subsequent discussion, all variables referenced are non-dimensional unless otherwise noted.

### 2.3. Numerical scheme

A brief summary of the numerical methodology employed in the study is provided here, and a detailed description is given in Basak & Sarkar (2006) and Brucker & Sarkar (2007). The non-dimensional Boussinesq form of the Navier–Stokes equations, (2.6)–(2.8), are solved using a staggered-grid method, where vector quantities are stored on the cell faces, and scalar quantities are stored at the cell centres. The spatial derivatives are evaluated using a second-order central difference stencil, and the temporal integration is performed with the low-storage explicit third-order Runge–Kutta method of Williamson (1980). A parallel multi-grid solver is employed to accelerate the convergence of the pressure Poisson equation. The number of relaxation sweeps at each level is successively increased during coarsening in order to accelerate the convergence of the multi-grid algorithm. A sponge region is employed near the  $x_2$  and  $x_3$  boundaries to control spurious reflections from internal waves, and other disturbances propagating out of the domain. The sponge layer takes the form of a Rayleigh damping function which is designed in such a way that it gradually relaxes the velocities and density to their respective values at the boundaries. This is accomplished by adding the explicit damping terms:

$$-\phi(x_i) [U_i(x_i, t) - U_{i,\infty}], \quad -\phi(x_i) [\rho(x_i, t) - \rho_\infty] \quad (2.9)$$

to the right-hand side of (2.7) and (2.8), respectively. Here, the free-stream velocity and density are  $U_{i,\infty} = [0, 0, 0]$  and  $\rho_\infty(x_3) = 1 - \rho_0 C^* x_3/D$  respectively. The function  $\phi(x_i)$  is constructed such that it increases quadratically from  $\phi = 0$  to  $\phi = A_s$  in a region of thickness  $L_s$ . In the DNS,  $L_s = D/2$  and  $A_s = 1$ . The sponge region is always sufficiently far from the wake during the entire simulation and therefore does not affect flow evolution in the region of interest.

Periodic boundary conditions are used in the streamwise ( $x_1$ ) direction for all variables. In the spanwise ( $x_2$ ) and cross-stream ( $x_3$ ) directions, Dirichlet and Neumann boundary conditions are used, in combination with the sponge layer, as follows:

$$u_i(\pm x_{2,3}) = 0, \quad p(\pm x_{2,3}) = 0, \quad \frac{\partial \rho}{\partial x_2}(\pm x_2) = 0, \quad \frac{\partial \rho}{\partial x_3}(\pm x_3) = -\rho_0 C^*/D. \quad (2.10)$$

#### 2.4. Initial conditions

Proper initial conditions are important since the shear production in a wake is small. Although there is some data on mean profiles and turbulent stresses, there is no dataset which characterizes the full state of the turbulence in the near wake region. The velocity cross-correlations are available, and thereby the turbulence production. Dommermuth *et al.* (2002) devised a method whereby the initial velocity was constructed as the sum of a mean field and prescribed fluctuating field. The constructed field was then subjected to an adjustment procedure in which the fluctuations were allowed to evolve with a fixed amplitude while the mean was held fixed. The resultant, post-adjustment, field was one in which the turbulence was realistic, as measured by the cross-correlation coefficient  $\langle u'_i u'_j \rangle / K$ , where  $K$  is the *t.k.e.*, the ' represents a fluctuation from the streamwise average (Reynolds average) and  $\langle \cdot \rangle$  denotes a streamwise average, all of which are discussed in more detail in §3.

The initial mean wake velocity profiles for the towed and self-propelled wake are, respectively,

$$\langle u_1 \rangle (r) = U_0 e^{-(1/2)(r/r_0)^2}, \quad (2.11)$$

$$\langle u_1 \rangle (r) = U_0 [1 - (1/2)(r/r_0)^2] e^{-(1/2)(r/r_0)^2}. \quad (2.12)$$

Here,  $U_0$  is the initial centreline velocity defect,  $r = \sqrt{x_2^2 + x_3^2}$  and  $r_0$  is the initial wake width and height. All of the wakes simulated here have the same peak velocity,  $U_0 = 0.11$ , and same radius,  $r_0 = 1/2$ . The initial velocity profile for both cases is axisymmetric with the radial variation as sketched in figure 1. Note that the area integral of (2.12) is zero corresponding to a wake with zero initial net momentum. Equation (2.12) was the same profile used in the LES simulations of Rottman *et al.* (2003) and compared well with the measured velocity profiles in the jet-driven disk experiments of Naudascher (1965).

Broadband velocity fluctuations are used with an initial spectrum given below by

$$E(k) = (k/k_0)^4 e^{-2(k/k_0)^2}, \quad (2.13)$$

where  $k_0 = 4.4$ . The energy spectrum peaks at a dimensional wavelength of  $4.4D$ , and corresponds to low- $Re$  turbulence. The energy spectrum at high wavenumbers is allowed to build up in time through nonlinear transfer during the initialization period. The initial intensity of the turbulence on the centreline,  $a = \langle u'_\alpha u'_\alpha \rangle_{CL}^{1/2}$  ( $\alpha = 1, 2, 3$  no summation implied), is given in table 1. The fluctuations are damped exponentially away from the centreline by multiplication of the fluctuating velocity field  $u'_i$  with the following radial damping function:

$$g(r) = a [1 + (r/r_0)^2] e^{-1/2(r/r_0)^2}, \quad (2.14)$$

which closely fits the spatial distribution of turbulence in the near wake in the experiments of Bevilaqua & Lykoudis (1978), Uberoi & Freymuth (1970) and was also used in the simulations of Dommermuth *et al.* (2002),

The initial fluctuations are generated following Rogallo (1981) where an isotropic divergence free velocity field is created in spectral space, such that it satisfies the spectrum given by (2.13). This method couples the velocity components, which shortens the time necessary in the adjustment procedure. As in Dommermuth *et al.* (2002), the fluctuations evolve with the mean held fixed until the maximum value of  $\langle u'_i u'_j \rangle / K \approx -0.25$ , signifying that the cross-correlation has increased to a level typical of shear flow turbulence. There are no density fluctuations imposed,  $\tilde{\rho}(x_i, 0) = 0$ . The effect of non-zero initial density perturbations was considered for the plane mixing

Case	$Re$	$Fr$	$Pr$	$a$	$N_1$	$N_2$	$N_3$	$L_1$	$L_2$	$L_3$	$t_f$
$TR50F04^1$	50 000	4	1	0.08	4096	1024	512	61.44	15.36	7.68	100
$SPR50F04^1$	50 000	4	1	0.08	4096	1024	512	61.44	15.36	7.68	100
$TR50F04^2$	50 000	4	1	N/A	1280	512	256	61.44	24.58	12.29	1500
$SPR50F04^2$	50 000	4	1	N/A	1280	512	256	61.44	24.58	12.29	1500
$TR50^1$	50 000	$\infty$	1	0.083	4096	512	512	61.44	7.68	7.68	30
$SPR50^1$	50 000	$\infty$	1	0.083	4096	512	512	61.44	7.68	7.68	40
$TR50^2$	50 000	$\infty$	1	N/A	1280	256	256	61.44	12.29	12.29	500
$SPR50^2$	50 000	$\infty$	1	N/A	1280	256	256	61.44	12.29	12.29	500
$TR10F02$	10 000	2	1	0.05	768	256	128	48.0	24.0	12.0	2000
$TR10F20$	10 000	20	1	0.05	768	256	128	48.0	24.0	12.0	2000

TABLE 1. Flow Parameters for simulated cases. *SP* denotes a self-propelled case and *T* denotes a towed case. Superscripts denote phase one ( $t < 100$ ) and phase two ( $t > 100$ ) of the simulations, as discussed in §2.5. Note that all lengths, velocities and times are all normalized by the twice the initial wake radius  $D$ , free-stream velocity  $U$  and  $T = U/D$  respectively.

layer in Brucker & Sarkar (2007) who found nearly identical temporal evolution of the shear layer with or without initial density fluctuations; this result was also observed by Riley & de Bruyn Kops (2003).

### 2.5. High- $Re$ simulations

DNS of turbulent flow typically requires  $\Delta x_i/\eta < 2 - 4$  for accurate calculation of second-order moments, where  $\eta$  is the Kolmogorov scale and calculated directly from the total non-dimensional dissipation rate as  $\eta \equiv (Re^3 \varepsilon)^{-1/4}$ . In this context,  $\eta$  is taken to be  $\min[\eta(x_2, x_3, t)]$ . The  $Re = 10\,000$  simulations are designed with a resolution of  $\Delta x_i/\eta < 4$  and the  $Re = 50\,000$  simulation with  $\Delta x_i/\eta < 2$ . To reduce the net computational cost, the decrease in Reynolds number with downstream distance typical of axisymmetric wake flows is exploited in the  $Re = 50\,000$  case. When the high resolution is no longer required, a regridding technique is employed as follows: During phase one,  $\Delta x_i = 0.015$  and spatial nodes  $N_i = [4096, 1024, 512]$  yielding a domain of  $L_i = [61.77, 15.36, 7.68]$ . By inspection of the  $Re = 10\,000$  results,  $\eta$  triples by  $t = 100$  and, without loss of accuracy, the velocity/density fields are regridded so that in phase two of the simulations  $N_i = [1280, 512, 256]$  and  $L_i = [61.77, 24.576, 12.288]$ . Note that the domain lengths in the spanwise and cross-stream directions are also increased to accommodate the increase of wake dimensions with time. In the spatial region where  $x_i > L_i^{old}$ , the velocity is set equal to  $L_i^{old} \exp[-(x_i - L_i^{old})^2]$  which smoothly decays the last plane of velocity in the old domain to zero in the new domain. This reduces the number of grid points required by a factor of 12.8 and allows the simulations to be continued to  $t = 1500$  with significantly less CPU time. The stratified  $Re = 50\,000$  simulations initially required  $2^{31}$  ( $\approx 2$  billion) grid points. In order to accommodate the large memory requirements, a three-dimensional domain decomposition method was employed to distribute rectangular sub-domains among many computational nodes. The data exchange between sub-domains was handled with the message passing interface (MPI) library. The first phase of each stratified  $Re = 50\,000$  simulation required 48 h on 1024 nodes of a Cray XT4 (49 152 h CPU time), and the second phase required 20 h on 128 nodes (2560 h CPU time). The  $Re = 50\,000$  unstratified simulations required half the domain size in the spanwise direction and required 48 h on 512 nodes (24 576 h CPU time) and 20 h on 64 nodes (1280 h CPU time) in the first and second phases, respectively.

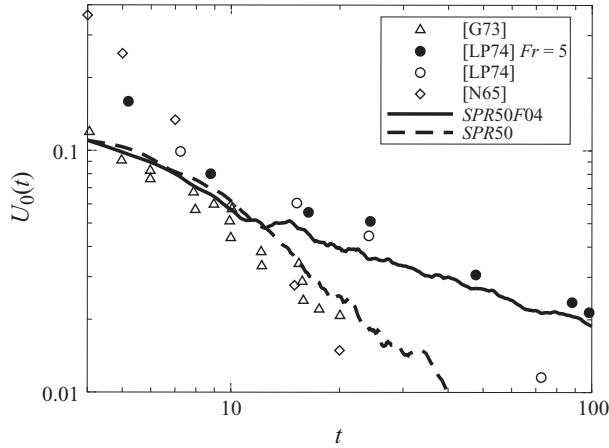


FIGURE 2. Evolution of peak velocity in cases *SPR50* and *SPR50F04*, compared to experiments. [G73] refers to the data from the experiments of Gran (1973). [LP74] refers to the data from the experiments of Lin & Pao (1974). [N65] refers to the data from the experiments of Naudascher (1965).

## 2.6. Parameters

The parameters of the simulated cases are given in table 1. For the towed  $Re = 10\,000$  cases the initial conditions were matched to the experiments of Bevilaqua & Lykoudis (1978) in order to validate the current numerical method against previous simulations.

In the towed  $Re = 50\,000$  simulations the initial conditions are matched to the data of Uberoi & Freymuth (1970). This choice was made to facilitate the comparison of simulations with higher turbulence levels to the existing high- $Re$  DNS simulations of Diamessis & Spedding (2006) and LES simulations of Dommermuth *et al.* (2002) which both used the Bevilaqua & Lykoudis (1978) data as initial conditions. For the self-propelled case, the initial conditions were modelled after the jet-driven disk experiments of Naudascher (1965), the available data was fit with a fourth-order interpolating polynomial. The peak velocity scale and streamwise fluctuation matched the corresponding values of 0.11 and 0.08 in the towed case at  $t_0 = (x - x_0)/D = 4$ .

The Froude numbers used in this study were chosen to be the minimum that would allow for a fully three-dimensional region in the near wake. This allowed for the maximum number of buoyancy periods for a given downstream distance. In light of the existing experimental evidence of Spedding, Browand & Fincham (1996), Spedding (1997) and Chomaz, Bonneton & Hopfinger (1993) which suggest the late wake scaling is independent of Froude number for  $Fr^R \equiv 2U/(ND) \gtrsim 4$  or in our notation  $Fr \equiv U/(ND) \gtrsim 2$ , and that there exists a region of vertical growth in the near wake for  $Fr \gtrsim 2$  (Lin, Boyer & Fernando 1992), the high- $Re$  simulations were run at  $Fr = 4$ .

## 2.7. Validation of self-propelled initial conditions

The peak defect velocity in the unstratified and stratified self-propelled cases, *SPR50* and *SPR50F04* respectively, are compared to the jet-driven experimental data of Naudascher (1965), and the propeller-driven experiments of Gran (1973) and Lin & Pao (1974). Figure 2, a plot of the defect velocity, shows that in both the stratified (thick — line) and unstratified (thick - - - line) cases the agreement with experiments is good. The experiment of Gran (1973) (open triangles) which had a defect velocity very

close to 0.11 at  $x/D = 4$  shows remarkably good agreement with simulation *SPR50* which used  $U_0 = 0.11$  and  $t_0 = 4$  as the starting point. The stratified simulation, case *SPR50F04*, also shows good agreement with the data set of Lin & Pao (1974) (closed circles) out to nearly  $t = 100$ .

### 3. Methods of data analysis

#### 3.1. Statistics

Since the flow is simulated in a temporally evolving domain, the data must be related to the spatial evolution. This is accomplished by assuming that the flow is statistically homogeneous in the streamwise direction and furthermore that

$$\widehat{\phi}(x_1) = \frac{1}{T_1} \int_0^{T_1} \phi(x_1 = X^M, t) dt \Leftrightarrow \frac{1}{L_1} \int_0^{L_1} \phi(x_1, t = T^M) dx_1 = \langle \phi \rangle(t), \quad (3.1)$$

where the overhat denotes temporal averaging, and angle brackets denote spatial averaging,  $L_1$  is length of the computational domain in streamwise direction,  $T_1$  is the duration of time averaging and  $X^M$  and  $T^M$  are the positions in space and time where the statistics match.

The Reynolds average, denoted with angle brackets,

$$u_i = \langle u_i \rangle + u'_i, \quad \rho = \langle \rho \rangle + \rho', \quad \tilde{\rho} = \langle \tilde{\rho} \rangle + \tilde{\rho}', \quad p = \langle p \rangle + p'. \quad (3.2)$$

is obtained by computing the average over the entire streamwise,  $x_1$ , direction, and the resulting Reynolds-averaged quantities are a function of time ( $t$ ) as well as the spanwise ( $x_2$ ), and cross-stream ( $x_3$ ) directions.

The total non-dimensional energy can be decomposed into kinetic energy and potential energy modes. In the present paper, we examine the non-dimensional kinetic energy of the wake defined as

$$E \equiv \frac{E^*}{\rho_0 U^2} = m.k.e. + t.k.e. = \frac{1}{2} \langle u_i \rangle \langle u_i \rangle + \frac{1}{2} \langle u'_i u'_i \rangle. \quad (3.3)$$

The evolution equations, given below, for the *m.k.e.* and *t.k.e.* are used to analyse and quantify of the exchange of energy between mean kinetic, turbulent kinetic and potential energy modes, the transport of kinetic energy away from the wake by internal waves, and the irreversible loss of kinetic energy by molecular diffusion.

#### 3.2. Mean kinetic energy

The mean kinetic energy, *m.k.e.*  $\equiv (\langle u_i \rangle \langle u_i \rangle) / 2$  evolves as

$$\frac{D(m.k.e.)}{Dt} = -P - \bar{\varepsilon} + \bar{B} - \frac{\partial T_i}{\partial x_i}. \quad (3.4)$$

Here,  $P$ , the production of *t.k.e.*, defined as

$$P \equiv -\langle u'_i u'_j \rangle \frac{\partial \langle u_i \rangle}{\partial x_j} = \underbrace{-\langle u'_1 u'_2 \rangle \frac{\partial \langle u_1 \rangle}{\partial x_2}}_{P_{12}} \underbrace{-\langle u'_1 u'_3 \rangle \frac{\partial \langle u_1 \rangle}{\partial x_3}}_{P_{13}} \underbrace{-\langle u'_2 u'_3 \rangle \frac{\partial \langle u_2 \rangle}{\partial x_3} - \langle u'_3 u'_2 \rangle \frac{\partial \langle u_3 \rangle}{\partial x_2}}_{\approx 0},$$

transfers energy between mean kinetic and turbulent kinetic modes.  $\bar{\varepsilon}$  is the dissipation of *m.k.e.*, defined as

$$\bar{\varepsilon} \equiv \frac{2}{Re_0} \langle S_{ij} \rangle \langle S_{ij} \rangle, \quad \langle S_{ij} \rangle = \frac{1}{2} \left( \frac{\partial \langle u_i \rangle}{\partial x_j} + \frac{\partial \langle u_j \rangle}{\partial x_i} \right),$$

$\partial T_i / \partial x_i$  is the transport of *m.k.e.*, defined as

$$T_i \equiv \langle u_j \rangle \langle u'_i u'_j \rangle + \langle u_i \rangle \langle p \rangle - \frac{2}{Re_0} \langle u_j \rangle \langle S_{ij} \rangle.$$

Here,  $\bar{B}$ , the mean buoyancy term, defined as

$$\bar{B} \equiv -\frac{1}{Fr^2} \langle \tilde{\rho} \rangle \langle u_3 \rangle,$$

transfers energy between mean kinetic and potential energy modes.

### 3.3. Turbulent kinetic energy

The *t.k.e.*, denoted from here on as  $K$  and defined as  $K \equiv \langle u'_i u'_i \rangle / 2$  evolves as

$$\frac{DK}{Dt} = P - \varepsilon + B - \frac{\partial T'_i}{\partial x_i}. \quad (3.5)$$

Here,  $\varepsilon$  is the dissipation of *t.k.e.*, defined as

$$\varepsilon \equiv \frac{2}{Re_0} \langle s'_{ij} s'_{ij} \rangle; \quad s'_{ij} = \frac{1}{2} \left( \frac{\partial u'_i}{\partial x_j} + \frac{\partial u'_j}{\partial x_i} \right),$$

$\partial T'_i / \partial x_i$  is the transport of *t.k.e.*, defined as

$$T'_i \equiv \frac{1}{2} \langle u'_i u'_j u'_j \rangle + \langle u'_i p' \rangle - \frac{2}{Re_0} \langle u'_j s'_{ij} \rangle.$$

The turbulent buoyancy flux  $B$  defined as

$$B \equiv -\frac{1}{Fr^2} \langle \tilde{\rho}' u'_3 \rangle,$$

transfers energy between turbulent kinetic and potential energy modes.

### 3.4. Velocity and length scales

In towed wakes, the cross-sectional area increases, and the mean streamwise velocity decreases. Owing to stratification, the spread of the wake is anisotropic and two separate measures of the thickness,  $r_2(t)$  in the horizontal and  $r_3(t)$  in the vertical, are computed by Gaussian function fits,  $U_0(t) \exp[-(1/2)(x_2 - x_2^0)^2 / r_2(t)^2]$  and  $U_0(t) \exp[-(1/2)(x_3 - x_3^0)^2 / r_3(t)^2]$ , to the mean streamwise velocity profiles,  $\langle u_1 \rangle(x_2, x_3, t)$ , along the horizontal and vertical centrelines of the wake, respectively.  $U_0(t)$  is defined as the maximum mean streamwise velocity, since the wake can meander around a mean position; this is 'not' identical to the streamwise velocity at  $(x_2, x_3) = (0, 0)$ . The horizontal and vertical wake centrelines pass through the point  $(x_2^0, x_3^0)$ , where  $U_0(t) = \langle u_1 \rangle(x_2^0, x_3^0)$ .

In order to compare the evolution of wake thickness between towed and self-propelled cases in a meaningful way, we introduce a generalized definition of wake thickness, valid for any velocity profile, by employing a second central spatial moment of the square of the mean streamwise velocity  $\langle u_1 \rangle^2(x_2, x_3, t)$  in the horizontal and vertical directions as follows:

$$R_\alpha^2(t) = A \frac{\int_C (x_\alpha - x_\alpha^c)^2 \langle u_1 \rangle^2 dC}{\int_C \langle u_1 \rangle^2 dC}, \quad x_\alpha^c(t) = \frac{\int_C x_\alpha \langle u_1 \rangle^2 dC}{\int_C \langle u_1 \rangle^2 dC}. \quad (3.6)$$

Here,  $\alpha = 2, 3$  and  $C$  is taken to be the area of the  $x_2$ - $x_3$  plane excluding the sponge region. The square of the mean streamwise velocity is employed instead of the

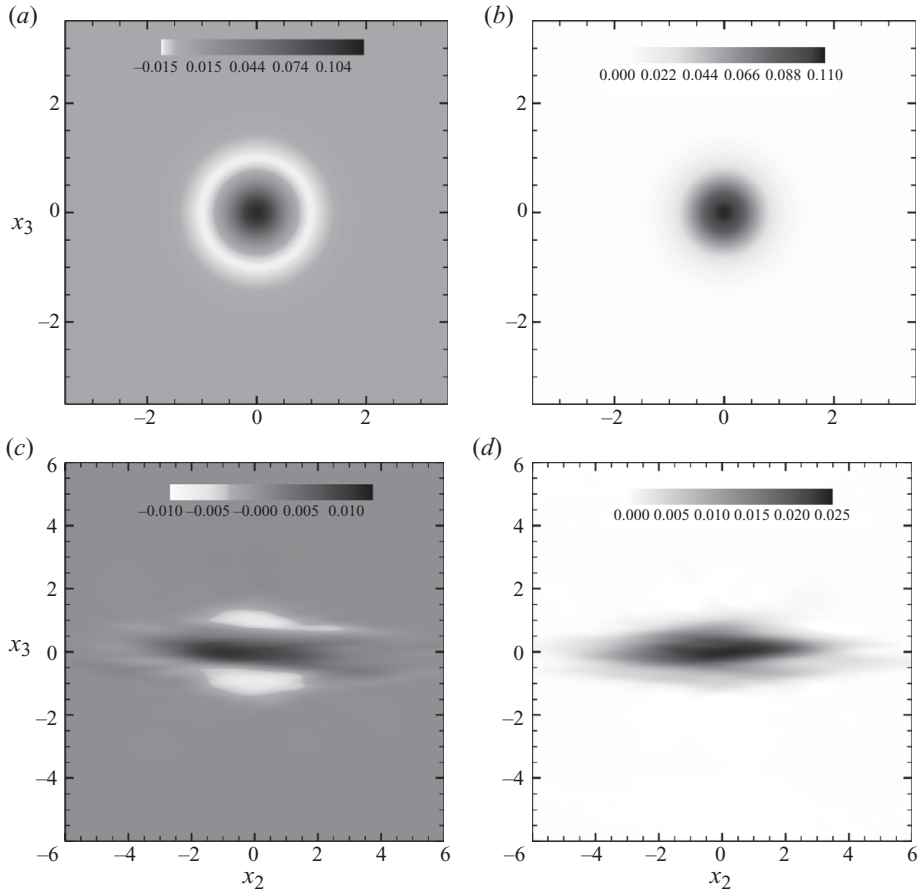


FIGURE 3. Mean velocity contours of stratified self-propelled (*a, c*) and stratified towed (*b, d*) wakes at  $Re = 50\,000$ . (*a, b*)  $t = t_0$ , (*c, d*)  $t = 500$ .

velocity in the above definition since the denominator of (3.6) could be zero for the self-propelled profile if the streamwise velocity were to be used. The choice of  $A = 2$  ensures that the definition of wake thickness in (3.6) gives  $R_2 = R_3 = r_0$ .

#### 4. Visualizations

The variation of mean velocity  $\langle u_1 \rangle(x_2, x_3, t)$ , a two-dimensional function for a given value of  $t$ , is illustrated by means of contours in figure 3. The  $t = t_0$  plot in figure 3(*a*) shows the negative velocity lobes present in the self-propelled wake. The mean velocity at a later time,  $t = 500$ , is depicted in figures 3(*c*) and 3(*d*) which show the flattening of the wake in the vertical direction common to both wakes. In case *SPR50F04*, figures 3(*a*) and 3(*c*), the negative velocity that initially surrounded the positive lobe remains coherent in the vertical direction but is wiped out along the horizontal centreline. This difference in the vertical structure of the stratified self-propelled wake relative to the towed wake has important consequences as will become clear later.

The vertical vorticity  $\omega_3$  at  $t = 500$ , is shown in figures 4(*a*) and 4(*b*) for cases *TR50F04* and *SPR50F04*, respectively. A detailed analysis of the vortex structures

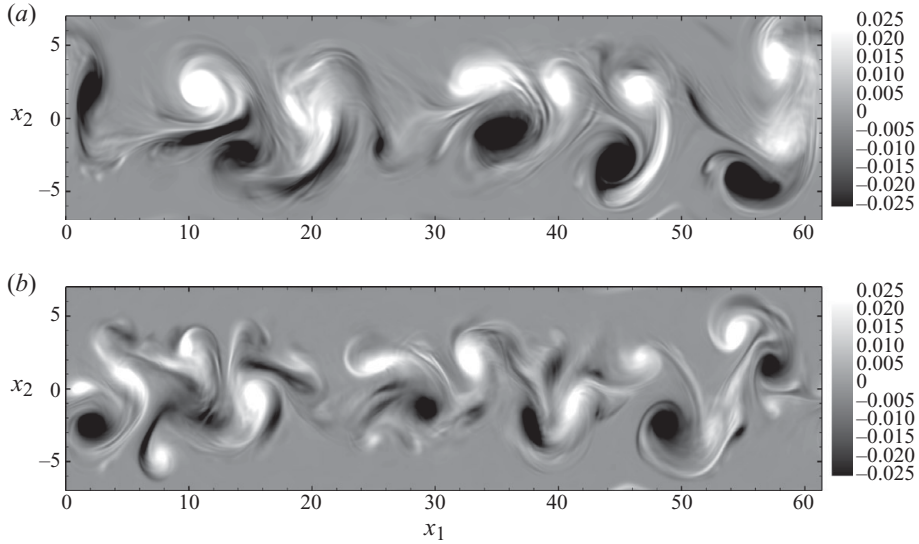


FIGURE 4.  $x_1$ - $x_2$  slice of instantaneous vertical vorticity field  $\omega_3$  on the horizontal plane  $x_3 = 0$  at  $t = 500$ : (a) Case *TR50F04*, (b) Case *SPR50F04*.

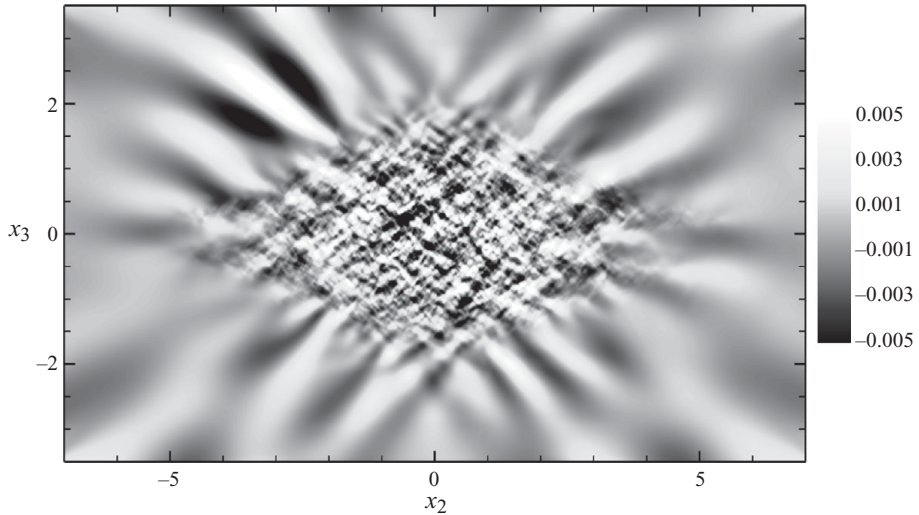


FIGURE 5. Internal wave field visualized by contours of  $\langle \partial u'_3 / \partial x_3 \rangle$ , case *SPR50F04* at  $t = 94$ .

is the subject of a follow-up study. In brief, coherent vortices are apparent and, as mentioned in the introduction, the presence of these vortices is one of the principal distinguishing features of stratified wakes. Lin & Pao (1979) noted that the vortices in the self-propelled case were smaller than those in the towed case, and our results are qualitatively similar. Meunier & Spedding (2006) and other previous studies have termed the vorticity disorganized and noted that it is contained in a finite band.

The stratified self-propelled wake has an associated internal wave field that has been observed in previous studies of the towed wake. The internal wave field shown in figure 5 at  $t \approx 100$  for the self-propelled case at  $Re = 50\,000$  exhibits the same characteristic pattern observed in towed wake simulations in the far field.

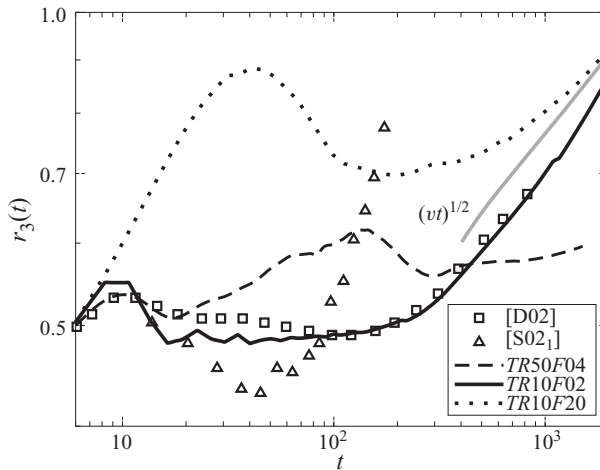


FIGURE 6. The evolution of the wake height,  $r_3(t)$ . [D02] refers to data from the simulations of Dommermuth *et al.* (2002),  $Re = 10\,000$ ,  $Fr = 2$ . [S02<sub>1</sub>] refers to data from the experiments of Spedding (2002),  $Re = 8000$ ,  $Fr = 2$ .

Before commencing the discussion of the differences between the towed and self-propelled cases in § 6, we digress briefly to discuss the evolution of the towed wake in a stratified fluid in § 5.

## 5. Towed wake

Case *TR10F02* which is a towed wake simulation with  $Re = 10\,000$  and  $Fr = 2$ , has an initial velocity field corresponding to the  $x/D = 6$  laboratory data of Bevilaqua & Lykoudis (1978) and is compared to the existing experimental data of Spedding *et al.* (1996), Spedding (1997), Spedding (2002), Bonnier, Bonneton & Eiff (1998) and simulations of Gourlay *et al.* (2001), Diamessis *et al.* (2005) and Dommermuth *et al.* (2002). Case *TR10F02* has the same fluid properties, flow parameters and initial turbulence levels as those used in the LES simulations of Dommermuth *et al.* (2002), since the latter simulation resolves nearly 95 % of the turbulent dissipation rate, the results are expected to be close in accuracy to a DNS, and very close agreement to case *TR10F02* is expected.

The vertical thickness  $r_3(t)$ , shown in figure 6 (— line, for *TR10F02*), exhibits an initial increase in the NW region,  $t < 10$ , similar to the  $t^{1/3}$  growth rate observed in unstratified wakes, followed by a suppression in the region,  $10 < t < 200$ , owing to buoyancy. In the late wake,  $t > 200$ , there is an increase of  $r_3(t)$ . The solid grey line in the region  $t > 200$  of figure 6(a) is proportional to  $\sqrt{\nu t}$ , where  $\nu = 1/Re_0 = 10^{-4}$ , providing evidence in support of the late wake vertical growth owing to viscous diffusion as proposed by Spedding (2002) and others. The increase of  $r_3(t)$  occurs earlier and is more pronounced in the laboratory data of Spedding (2002) starting at  $t = 80$  versus  $t = 300$  in the present DNS. The differences are in part due to the different definitions of vertical wake thickness. Spedding (2002) takes the vertical length scale of the wake to be the length at which mean velocity is 20 % of the peak value. Large differences between simulation and experimental data on  $r_3(t)$  were also noted in the simulations of Dommermuth *et al.* (2002).

The evolution of the horizontal thickness  $r_2(t)$ , shown in figure 7 (— line, for *TR10F02*), shows the NW, NEQ and quasi-two-dimensional phases as discussed in

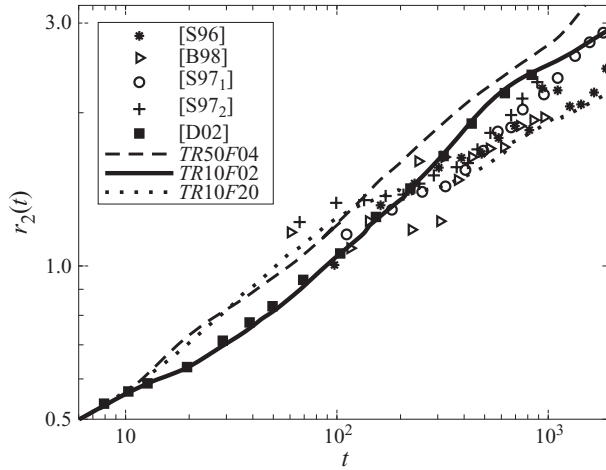


FIGURE 7. The evolution of the wake width  $r_2(t)$ . Symbols as in figure 6, and additional symbols as follows: [S96] refers to the data from the experiments of Spedding *et al.* (1996),  $Re = 5000$ ,  $Fr = 4.0$ ; [S97<sub>1</sub>] refers to the data from the experiments of Spedding (1997),  $Re = 5100$ ,  $Fr = 5$ ; [S97<sub>2</sub>] refers to the data from the experiments of Spedding (1997),  $Re = 5800$ ,  $Fr = 10$ ; [B98] refers to data from the experiments of Bonnier *et al.* (1998),  $Re = 8000$ ,  $Fr = 3$ .

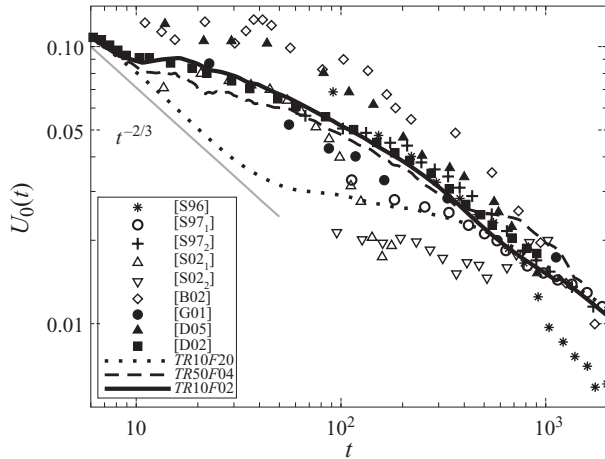


FIGURE 8. Evolution of peak defect velocity  $U_0(t)$ . Symbols as in figures 6 and 7 and additional symbols as follows: [S02<sub>2</sub>] refers to data from the experiments of Spedding (2002),  $Re = 8000$ ,  $Fr = 8$ ; [B02] refers to data from the experiments of Bonnier & Eiff (2002),  $Re = 6900$ ,  $Fr = 3$ ; [G01] refers to data from the simulations of Gourlay *et al.* (2001),  $Re = 10\,000$ ,  $Fr = 5$ ; [D05] refers to data from the simulations of Diamessis *et al.* (2005),  $Re = 20\,000$ ,  $Fr = 2$ .

the introduction. In the near wake,  $t < 10$ , the growth is similar to the unstratified rate of  $t^{1/3}$ . In the region  $10 < t < 200$  the growth rate is  $t^{0.31}$  and in the region  $200 < t < 500$  the growth rate is  $t^{0.46}$  consistent with the growth rates in the range of  $t^{0.25}$ – $t^{0.40}$  which were observed during the NEQ phase in the experiments of Spedding *et al.* (1996). After  $t \approx 700$  the growth in the horizontal is  $t^{0.23}$  very close to the  $t^{1/4}$  rate in the quasi-two-dimensional phase reported in Spedding (1997).

The evolution of the peak defect velocity  $U_0(t)$ , figure 8 (— line, for  $TR10F02$ ), shows evidence of the stages identified during the evolution of the horizontal and

vertical thicknesses. In the region  $t < 10$ , there is a near wake stage with a decay in mean velocity close to the unstratified rate,  $t^{-2/3}$ . During  $10 < t < 200$ , the wake adjusts to buoyancy effects and the velocity evolution exhibits an initial short plateau ( $10 < t < 20$ ) which was called an accelerated collapse (AC) phase by Bonnier & Eiff (2002), followed by a velocity decay rate of  $t^{-0.26}$  which is slower than the unstratified rate,  $t^{-2/3}$ , and close to the  $t^{-1/4}$  rate observed in the experiments of Spedding (1997) and simulations of Diamessis *et al.* (2005). During the time  $200 < t < 500$  the velocity decay rate is  $t^{-0.69}$  which is in good agreement with the scaling exponent of  $t^{-0.62}$  that is observed for the  $Re = 10\,000$  data sets in the experiments of Spedding (1997) and nearly identical to that in the simulations of Dommermuth *et al.* (2002).

Before commencing the discussion of the differences between the towed and self-propelled cases, we summarize the differences observed in a towed wake by varying  $Re$  and  $Fr$ . The peak defect velocity in the high- $Re$  towed case  $TR50F04$  is shown in figure 8, (--- line). With increasing  $Re$ , a change in the type and duration of the NEQ regime is observed. In the  $Re = 50\,000$  case there is a very clear plateau between  $400 < t < 700$  after which the decay rate in case  $TR50F04$  is  $t^{-0.64}$  within the range reported in Spedding (1997) for the quasi-two-dimensional phase. The effect of the Froude number is illustrated with case  $TR10F20$  (dotted line), a towed wake simulation with  $Re = 10\,000$  and  $Fr = 20$ , which has a relatively weaker stratification. The duration of the essentially unstratified behaviour in the NW stage is longer. The transition to the NEQ regime occurs at  $t \approx 200$ , later than the  $t \approx 40$  and  $t \approx 20$  values observed in the  $Fr = 4$  and  $Fr = 2$  simulations. The values of the transition time, when scaled with  $N$ , collapse to  $Nt \approx 5$  for all three cases. This result provides further support to the  $Nt$  scaling that was deduced in the previous laboratory experiments of Spedding *et al.* (1996) and Bonnier & Eiff (2002). Cases  $TR10F02$ ,  $TR10F20$  and  $TR50F04$  are plotted in figure 9 as  $U_0(t)Fr^{2/3}$  versus  $Nt$  which was proposed by Spedding (1997) to collapse the effect of  $Fr$ . Figure 9 shows that cases with different  $Fr$  do indeed collapse when plotted in this fashion. However, between  $Nt \approx 100$  and  $Nt \approx 250$  there is a distinct plateau for cases with  $Re = 50\,000$ – $100\,000$ , that is not evident in cases with  $Re = 5000$ – $10\,000$ . The high- $Re$  simulations of Diamessis & Spedding (2006) (data shown as symbols figure 9) also exhibit this plateau; however, it was ‘not’ observed in the LES of Dommermuth *et al.* (2002).

The peak defect velocity is shown for case  $TR50F04$  in figure 10. The velocity scale based on the mean integrated (over  $C$  the  $x_2$ – $x_3$  cross-section excluding the sponge region) streamwise kinetic energy,

$$U_1^{m.k.e.} = \left( \frac{1}{2C} \int_C \langle u_1 \rangle \langle u_1 \rangle dC \right)^{1/2}, \quad (5.1)$$

is also shown and it is noted that it is a good surrogate for the peak streamwise defect velocity. For  $8 < t < 120$  or  $2 < Nt < 30$  the data is best fit by  $t^{-0.24}$  well within the range of  $-0.25 \pm 0.04$  given by Spedding (2002) for the scaling the NEQ regime. When  $t > 1000$  or  $Nt > 250$ , the data is fit best by  $t^{-0.64}$  which is towards the lower part of the range,  $-0.76 \pm 0.12$ , given by Spedding (2002) for the quasi-two-dimensional phase. However, the plateau noted in figure 9 for  $100 < Nt < 250$  in case  $TR50F04$  is actually part of a larger region  $30 < Nt < 250$  which is non-equilibrium in the sense that the evolution is neither similar to the unstratified wake (NW) nor to the quasi-two-dimensional wake. We will call this non-equilibrium subregion,  $30 < Nt < 250$ , as NEQ<sup>2</sup> to distinguish it from the NEQ<sup>1</sup> subregion that occurs earlier,  $5 < Nt < 30$  in our simulation with the  $-0.25 \pm 0.04$

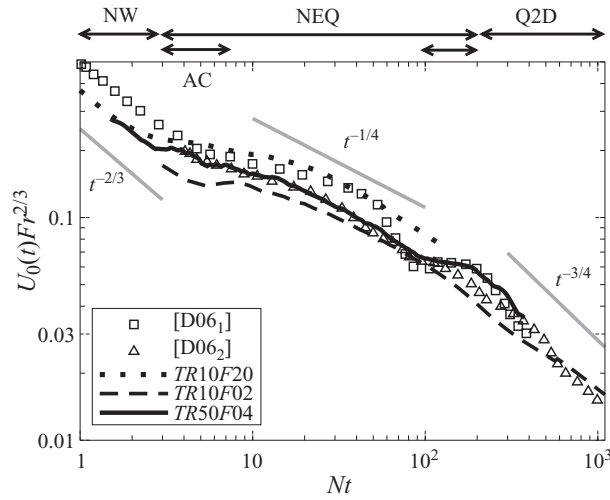


FIGURE 9. Evolution of peak defect velocity plotted as  $U_0(t)Fr^{2/3}$  versus  $Nt$ . [D06<sub>1</sub>] corresponds to the data from the simulations of Diamessis & Spedding (2006),  $Re = 5000$  and  $Fr = 2$ . [D06<sub>2</sub>] corresponds to the data from the simulations of Diamessis & Spedding (2006),  $Re = 100\,000$  and  $Fr = 8$ .

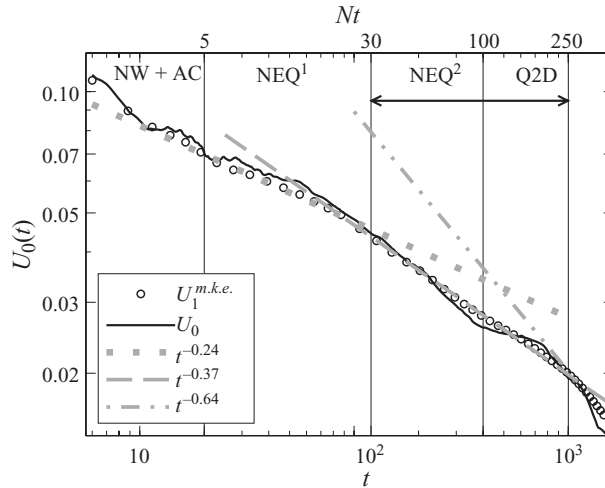


FIGURE 10. The various stages in the towed wake, case  $TR50F04$ , that are exhibited by the peak wake defect velocity,  $U_0(t)$ , and the velocity scale based on the mean (integrated over  $C$  the  $x_1-x_2$  cross-section excluding the sponge region) streamwise kinetic energy,  $U_1^{m.k.e.}(t)$ .

power-law exponent identified by Spedding (2002). Attention is now focused on a comparison between a towed and a self-propelled wake in stratified and unstratified fluids.

### 6. Comparison between self-propelled and towed wake

The discussion in this section focuses on the evolution of the peak streamwise velocity,  $U_0(t)$ , and wake dimensions,  $R_2(t)$  and  $R_3(t)$  in stratified and unstratified fluids, which are discussed in figures 11 and 12. Figures 11 and 12 and many of

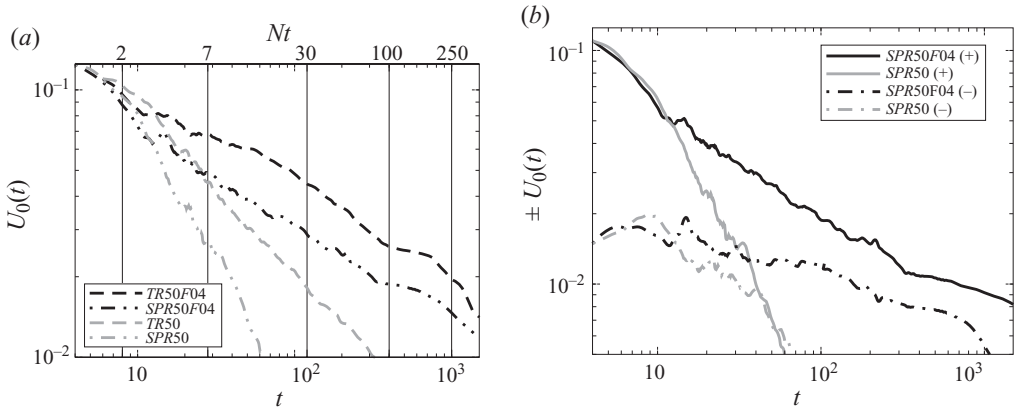


FIGURE 11. (a) Evolution of peak velocity difference in the towed and self-propelled wakes. (b) Evolution of peak positive and negative velocities in self-propelled wakes. Unstratified cases are shown in grey and stratified in black here and in later figures comparing these four cases.

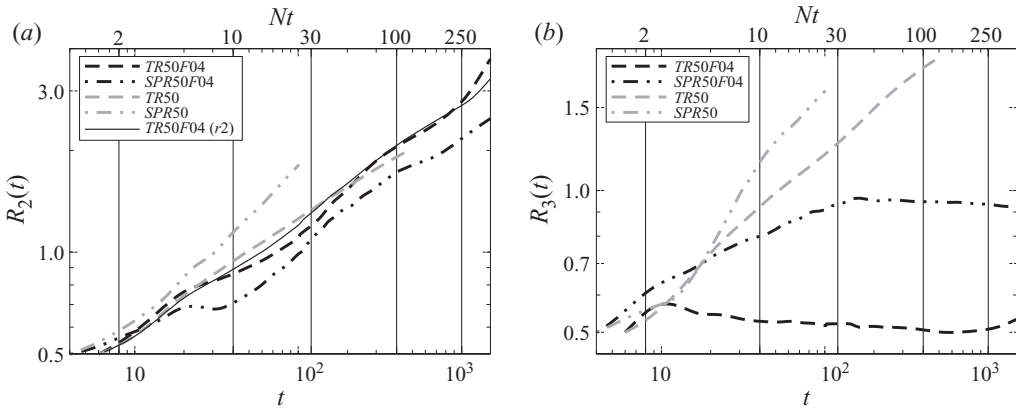


FIGURE 12. Evolution of wake thickness, defined by (3.6), in  $Re = 50\,000$  simulations: (a)  $R_2(t)$ , (b)  $R_3(t)$ . Stratified cases are shown in black and unstratified in grey.

the subsequent figures show results from the four high- $Re$  simulations: stratified cases  $TR50F04$  and  $SP50F04$ , and unstratified cases  $TR50$  and  $SPR50$ . We adopt the convention of black lines for stratified and grey lines for unstratified cases in such figures. The line type is dashed for the towed cases and dash-dot-dot for the self-propelled cases.

### 6.1. Stratified

The discussion is now turned to  $TR50F04$  and  $SPR50F04$ , that is, the towed and self-propelled simulations with  $Re = 50\,000$  and  $Fr = 4$ . The peak defect velocities are shown in figure 11(a); note that for case  $SP50F04$  the peak defect velocity is taken to be the most positive velocity minus the most negative velocity. The peak velocity decays more rapidly in the self-propelled case  $SP50F04$ , when compared to the towed case  $TR50F04$ . The largest differences in the growth rate occur during  $4 < t < 30$ . The subsequent decay rate during  $50 < t < 700$  is similar between the self-propelled and towed cases, albeit with the velocity in the self-propelled case being lower owing to the

differences before  $t = 30$ . There is an increase in the peak velocity in the self-propelled case around  $t = 15$ , the towed case shows a reduction in decay rate around this time. The AC stage proposed by Bonnier & Eiff (2002) to occur before the NEQ stage during  $2 < Nt < 7$  is consistent with the observed change in decay rate around  $t = 15$  ( $Nt \approx 4$ ). Figure 11(b) shows both the most positive and most negative values (note that the negative of the minimum is plotted since the ordinate is logarithmic) of  $\langle u_1 \rangle(x_2, x_3, t)$  for self-propelled cases. Inspection of figure 11(b) shows that, in the stratified self-propelled wake, the peak negative velocity decays at a much lower rate compared to the positive velocity until  $t \approx 700$ , at which point the decay rate becomes significantly larger. A detailed discussion of the mechanism by which the multi-signed structure of the self-propelled velocity profile is preserved and the conditions under which it is expected to survive is given in § 7.1.

We now turn to the horizontal and vertical dimensions of the wake. In figure 12(a), the thin solid line corresponding to the Gaussian fit and the black line corresponding to (3.6) show similar behaviour, both corresponding to the stratified towed case *TR50F04*. This, in conjunction with the towed unstratified cases (grey dashed line) shown in figure 12(a)–12(b) growing as  $t^{1/3}$ , the rate predicted by self-similarity, shows the suitability of (3.6) to compute wake dimensions. The evolution of  $R_2(t)$  and  $R_3(t)$  in figure 12 is now compared between self-propelled and towed wakes in a stratified fluid. The evolution of  $R_2(t)$  in self-propelled case *SPR50F04* is similar to that in the towed case *TR50F04* during  $t < 20$ . Between  $20 < t < 100$  there is a distinct plateau in the self-propelled case, with the stratified towed case showing a distinctly larger growth of  $R_2(t)$ . Between  $100 < t < 700$  the growth rates between the towed and self-propelled cases are similar. For  $t > 700$  the towed case shows a larger growth compared to the self-propelled case. As shown in figure 12(b), the evolution of  $R_3$  in case *SPR50F04* is substantially different than in case *TR50F04*. In particular, the vertical thickness of the self-propelled wake is substantially larger than that of the towed wake for all times. In the towed case, a near wake region is evident with a peak around  $t = 12$ . The collapse of the wake lasts until around  $t = 700$  at which time there is a slight growth. The self-propelled case shows three distinct regimes: (i) during  $t < 10$  there is a growth rate that is larger than the unstratified case, (ii) there is a secondary growth region between  $10 < t < 200$  where the rate is slower than the unstratified rate but significantly higher than that observed in the towed case and (iii) for  $t > 200$ , the vertical extent of the wake changes very slowly. It is worth noting that the viscous transport of momentum in a multi-inflectional velocity profile will not necessarily increase the thickness of the profile as it does when the velocity profile has only a single inflection point, since momentum from the outer region can be transported into the inner region and vice-versa. Inspection of figure 3 shows that the visual wake thickness is consistent with and proportional to  $R_2$  and  $R_3$ . The bottom frames of figure 3 roughly give wake dimensions of  $7 \times 4$  in the self-propelled case which is essentially  $4R_2$  by  $4R_3$  computed by (3.6). The same holds for the towed case where a rough estimate from figure 3 yields  $10 \times 2$  again essentially  $4R_2$  by  $4R_3$  computed by (3.6).

The peak defect velocity is shown for case *SPR50F04* in figure 13. The velocity scale based on the mean integrated streamwise kinetic energy,  $U_1^{m.k.e.}(t)$  (5.1), is also shown in the figure. Although, the peak velocity and mean streamwise kinetic energy evolved similarly in the towed case (see figure 10) the defect velocity scale,  $U_0(t)$  does not accurately reflect the decay in the streamwise kinetic energy in the self-propelled case. Interestingly, the stages identified in case *TR50F04*, a towed wake simulation, can in large part be identified in the self-propelled case. Figure 13 shows changes in

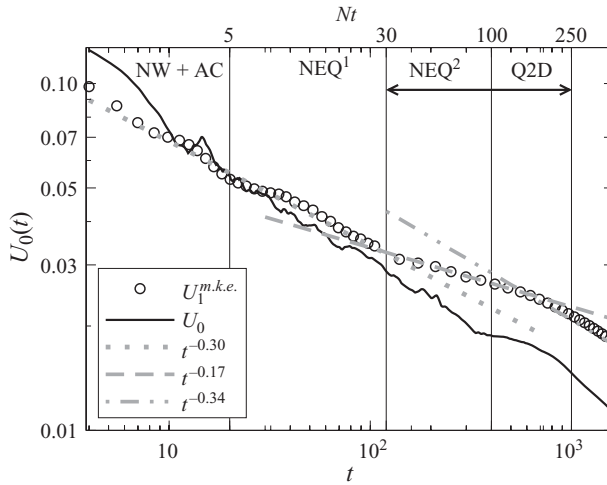


FIGURE 13. The various stages in the self-propelled wake, case *SPR50F04*, that are exhibited by the peak wake defect velocity,  $U_0(t)$ , and the velocity scale,  $U_1^{m.k.e.}(t)$  based on (5.1).

the decay rate of the streamwise velocity at similar times to those found in the towed case.

### 6.2. Unstratified

Here, we turn to a comparison of the unstratified self-propelled (case *SPR50*) and towed (case *TR50*) wakes. In figure 11(a) the peak defect velocity  $U_0(t)$  decays faster in the unstratified cases. Furthermore the *SPR50* case exhibits faster decay relative to *TR50*. The evolution of  $U_0$  follows closely to  $t^{-2/3}$  for the towed case. Figure 11(b), a plot of the self-propelled cases, shows that after  $t \approx 12$  there are significant differences between the stratified (black curves) and unstratified (grey curves) results. In the unstratified case, the positive and negative velocities decay faster and by  $t = 100$  their values become small and approximately equal, and the decay of the mean wake is almost complete. It is interesting to note in figure 12(a) that the growth of  $R_2$  is similar between the towed unstratified and stratified cases. However, this trend is not maintained in the self-propelled case and, for all time,  $R_2$  is smaller in the stratified case.

The important results so far can be summarized as follows. One, the presence of stratification allows the self-propelled wake to exist for a significantly longer time. Two, the multi-inflectional structure of the mean velocity profile in the vertical direction is preserved in the stratified self-propelled case. Three, in the near wake the peak velocity in the self-propelled wake decays faster than in the towed wake, and the thickness grows more in the vertical direction. Four, after this initial region where significant differences are observed, the growth in the horizontal thickness and the decay in the peak defect velocity occur at similar rates; whereas the vertical thickness continues to increase in the self-propelled case compared to a decrease in the towed case. Clearly, some of these differences such as the drastically different initial decay rate of mean velocity between the self-propelled and towed cases are due to the shape of the mean profile, whereas the large differences in the vertical thickness  $R_3$  are due to both the combination of the shape of the mean velocity profile and the presence of stratification. In the next section we consider the energetics of mean and fluctuating

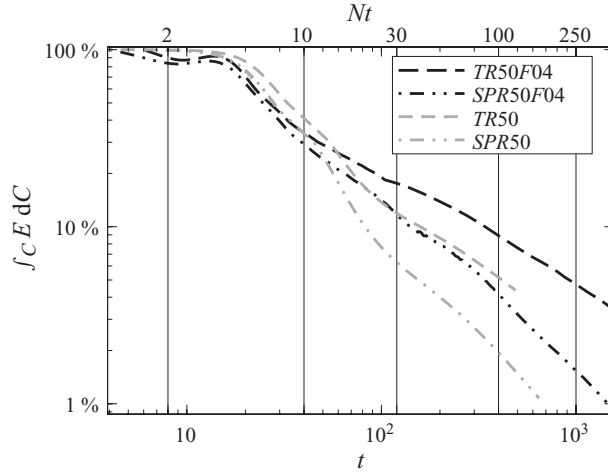


FIGURE 14. Evolution of the volume integrated kinetic energy as a percentage of the initial, for towed cases  $TR50F04$  and  $TR50$ , and self-propelled cases  $SPR50F04$  and  $SPR50$ .

components with the aim of further isolating the effects of the multi-inflectional velocity profile and of stratification.

## 7. Total kinetic energy

Figure 14 shows the evolution of the total kinetic energy given by (3.3). At  $t = 1500$  3% of the initial kinetic energy remains in the towed case whereas 1% remains in the self-propelled case. This is consistent with the faster decay rate of the peak defect velocity in the self-propelled wake and indicates that self-propelled wakes do dissipate energy faster than towed wakes.

Figure 15 shows the partitioning of total kinetic energy into mean and fluctuating quantities. Initially, in all cases most of the energy resides in  $t.k.e.$ . This is typical of wake flows in stratified and unstratified fluids (Uberoi & Freymuth 1970; Bevilaqua & Lykoudis 1978; Dommermuth *et al.* 2002) since the fluctuating velocity components are between 40% and 80% of the mean velocity and have a larger spatial extent. Comparing the dashed black and grey lines (with circles) between figures 15(a) and 15(b), it is observed that the  $m.k.e.$  in the self-propelled case can be a significant portion of the total energy at late time in the stratified case whereas it always remains at less than 10% in the unstratified case, showing that stratification preserves the  $m.k.e.$ . In the towed case, the  $m.k.e.$  in both the stratified and unstratified cases accounts for a larger amount of the total kinetic energy when compared to the self-propelled cases.

Figure 16 shows the evolution of  $R_{E3}(t)$  which is defined by replacing  $\langle u_1 \rangle^2$  with  $E \equiv m.k.e. + t.k.e.$  in (3.6). The scale  $R_{E3}(t)$  characterizes the vertical dimension of the fluid region disturbed from the background quiescent state by the presence of the wake. The evolution of  $R_{E3}(t)$  is similar between the towed and self-propelled wake until  $t = 20$ , at which point  $R_{E3}(t)$  grows at a faster rate in the self-propelled case, reaching a peak value 50% greater than the towed case at  $t = 350$ . After  $t = 350$ , both cases show a dramatic reduction. The rapid decrease in  $R_{E3}(t)$  in both cases corresponds to the plateau observed in the defect velocity, shown in figure 11(a).

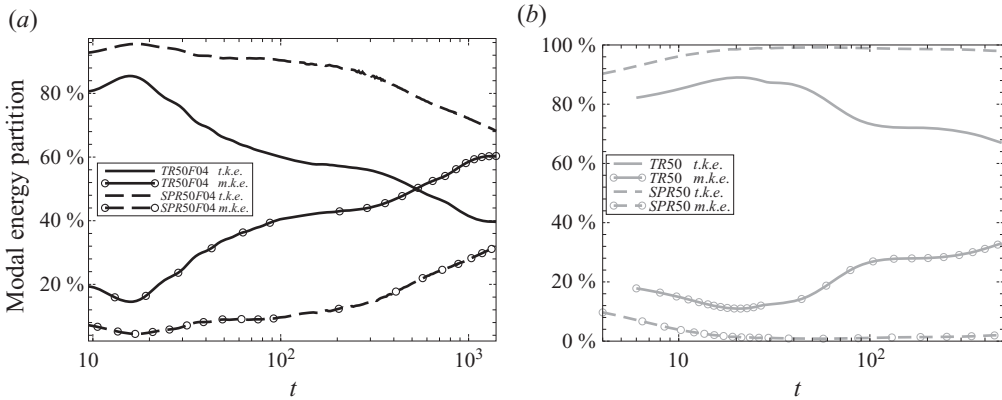


FIGURE 15. Partitioning of kinetic energy between *m.k.e.* and *t.k.e.* modes in the  $Re = 50\,000$  simulations: (a) stratified, (b) unstratified (solid lines correspond to towed cases and dashed lines to self-propelled cases).

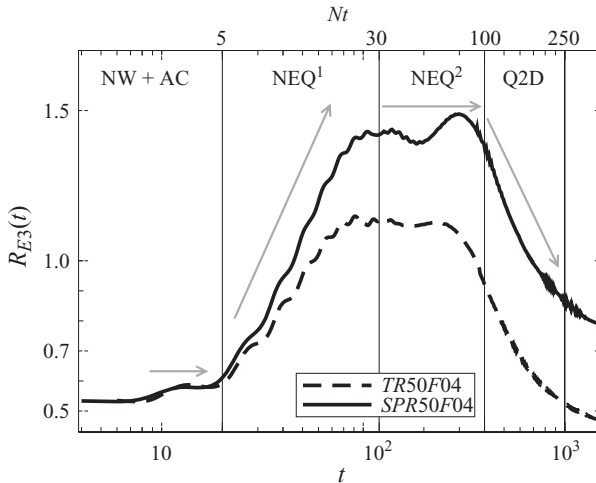


FIGURE 16. Comparison of the vertical extent,  $R_{E_3}(t)$ , of the region of fluid disturbance in the towed and self-propelled wake simulations at  $Re = 50\,000$ .

It is illustrative to consider the spatial distribution of the total energy which is shown in figure 17(a, c) (self-propelled) and figure 17(b, d) (towed) at  $t = t_0, 1000$ . The initial spatial distribution of energy is nearly identical between the two cases. The larger value of  $R_{E_3}(t)$  at a later time in the self-propelled case can be seen by comparing between figures 17(c) and 17(d). The outer lobes of negative velocity, previously identified in figure 3, can contain significant energy, approximately 50%, of that at the centreline. Clearly, there are similarities as well as significant differences between the distributions of energy in the two cases, i.e. the spread is anisotropic with a significantly greater spread in the horizontal compared to the vertical in both cases, and the presence/absence of the lobed structure in the self-propelled/towed cases. To explain the differences in decay rates, partitioning, and spatial distribution of total kinetic energy, it is useful to consider *m.k.e.* and *t.k.e.* as done in § 7.1 and § 7.2, respectively.

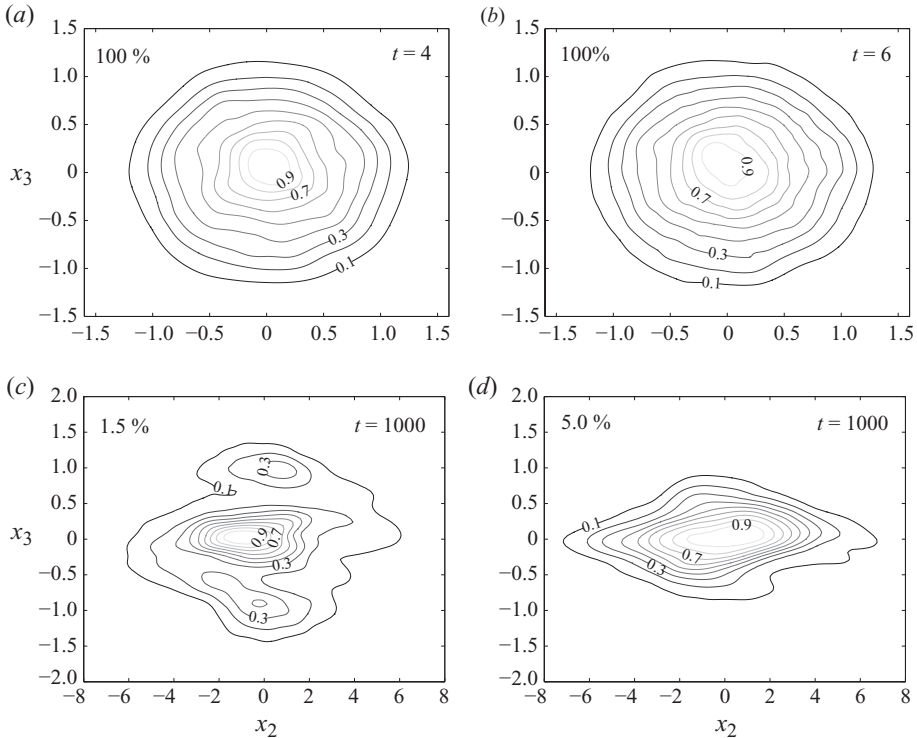


FIGURE 17. Contours of total kinetic energy,  $E \equiv m.k.e. + t.k.e.$ . Self-Propelled (*a, c*) and towed (*b, d*) at  $t = t_0$  (*a, b*),  $t = 1000$  (*c, d*). The maximum contour level is given in top left corner as a percentage of the initial maximum kinetic energy, 0.015. The dimensional scale is  $\rho_0 U^2$ .

### 7.1. Evolution of mean kinetic energy

The *m.k.e.* a function of  $(x_2, x_3, t)$ , is compared between self-propelled and towed cases with and without stratification. The initial value of *m.k.e.* in the self-propelled wake is half that of the towed case. This difference is due to the shape of the self-propelled velocity profile, (2.12), compared to the Gaussian shape of a towed wake profile, (2.11). The initial centreline velocity,  $U_0(t=0)$ , and initial radius,  $r_{2,3}(t=0) = r_0$ , were chosen to be the same in both cases. The decision to set  $r_0$  and  $U_0$  equal in the self-propelled and towed cases leads to high mean gradients in the self-propelled case, this can be seen by comparing the derivatives of (2.11)–(2.12). In § 6.1 it was shown that the peak streamwise velocity (see figure 11*a*), is smaller in the self-propelled wake relative to the towed wake, a result also observed in previous laboratory experiments (Higuchi & Kubota 1990; Sirviente & Patel 2000; Meunier & Spedding 2006). We offer the following possible explanation: the shape of the mean velocity profile is qualitatively different between the self-propelled and towed cases, with the self-propelled case having larger mean shear which results in an initially higher production in the self-propelled case versus the towed case. In the unstratified self-propelled case, turbulence tends to smooth regions of high mean gradients, and is a sink of *m.k.e.* and will therefore seek to reduce the gradients in the mean velocity, and transition the flow to the lowest energy configuration respecting the conservation of momentum. In the unstratified towed case, it is expected (Tennekes & Lumley 1972) that the lowest energy state will be very near a Gaussian profile containing the same momentum as the initial disturbance. In the self-propelled case the lowest energy configuration with

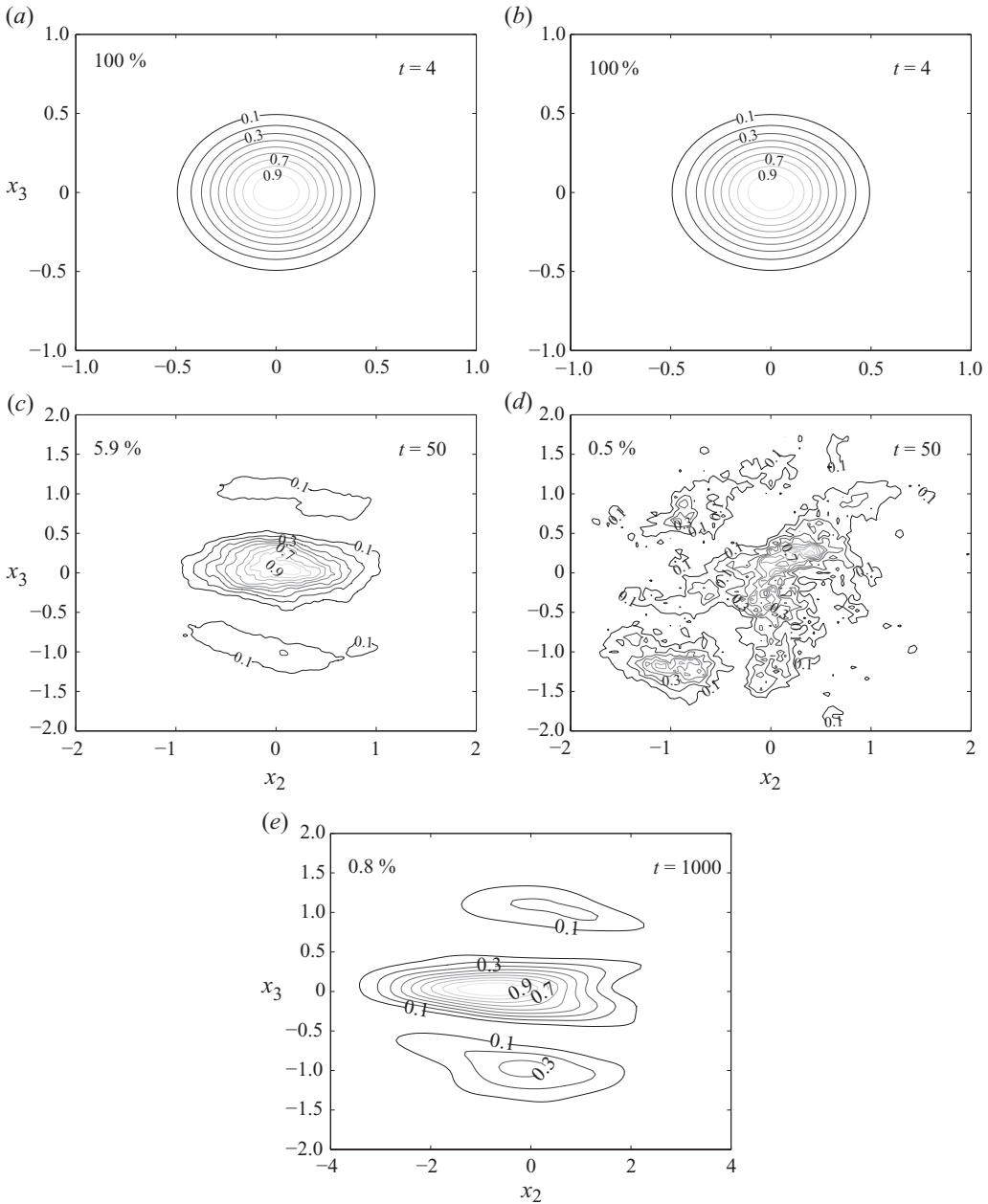


FIGURE 18. Contours of  $m.k.e.$  in the self-propelled cases at  $t = t_0$  (a, b)  $t = 50$  (c, d) and  $t = 1000$ . Stratified case *SPR50F04* shown in (a), (c) and (e) and unstratified case *SPR50* in (b), (d). The maximum contour level is given in the top left corner as a percentage of the initial maximum  $m.k.e.$ , 0.0061. The dimensional scale is  $\rho_0 U^2$ . The unstratified case has negligible energy at  $t = 1000$  and is therefore not shown.

the same amount of momentum (zero) is one in which  $\langle u_i \rangle = 0$ . Figure 18(b, d) shows the  $m.k.e.$  in case *SPR50*, the unstratified self-propelled case, at  $t = t_0$  (figure 18b), and  $t = 50$  (figure 18d). There is no discernible structure to the  $m.k.e.$  contours at  $t = 50$ . Clearly, the  $m.k.e.$  decays rapidly towards the zero velocity state in the unstratified

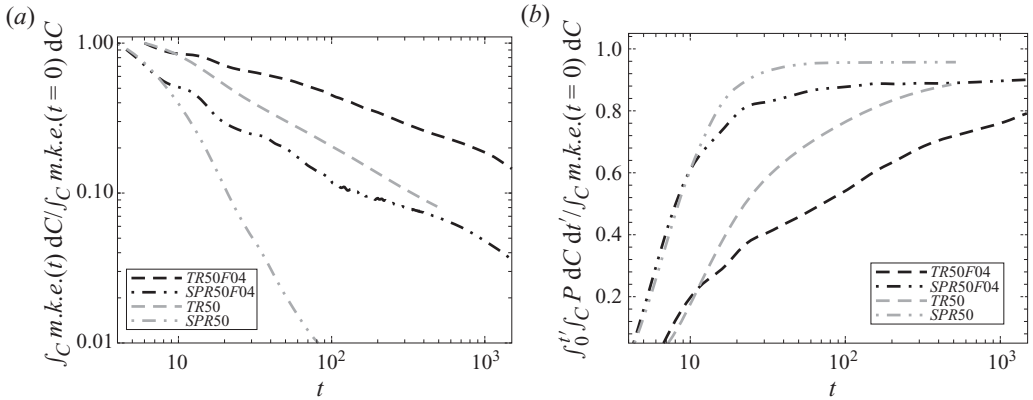


FIGURE 19. (a) Evolution of *m.k.e.* (b) Cumulative integral of production normalized by initial mean kinetic energy,  $m.k.e._0 \equiv \int_C m.k.e. dC(t=0)$ .

self-propelled case. In contrast, the state of  $\langle u_i \rangle = 0$  is not achieved in the stratified self-propelled case even at  $t=1000$ . Figure 18 shows there is a spatial pattern in the distribution of *m.k.e.* at  $t=1000$  for the self-propelled (figure 18*a,c,e*) cases. The peak value of *m.k.e.* at  $t=50$  in the unstratified case is 0.5% of the initial maximum *m.k.e.*, whereas the peak value of *m.k.e.* in the stratified case at  $t=1000$  is 0.8% of the initial maximum *m.k.e.*. Clearly, the decay in unstratified fluids is significantly faster than in the corresponding stratified cases. The self-propelled unstratified wake has less than 1% of the initial *m.k.e.* remaining by  $t=100$ . To proceed, the terms in the balance of *m.k.e.*, (3.4), are compared by integrating the streamwise average over the  $x_2$ - $x_3$  computational domain, excluding the sponge region ( $\int_C dC$ ). The dominant term is the turbulent production. The mean dissipation accounts for 5% of the loss of *m.k.e.*, in the stratified cases, by  $t=1500$ . The effect of turbulent production on the decay of *m.k.e.* is shown in figure 19(b) where the cumulative integral of the production,

$$\int_C \int_0^t P dC dt, \quad (7.1)$$

normalized by  $m.k.e._0 \equiv \int_C m.k.e.(t=0) dC$  is shown as a function of  $t$ . In the unstratified self-propelled case the ratio is 0.96 by  $t=40$  where it remains, showing that in the absence of stratification, almost all of the loss of *m.k.e.* in high-*Re* unstratified self-propelled wakes is due to the production of turbulence.

Figures 19(a) and 19(b) reveal why the *m.k.e.* is preserved in the presence of stratification. The self-propelled stratified and unstratified cases evolve similarly until  $t=10$  at which point the stratified case shows a reduced growth, reaching only 0.82 by  $t=40$ . This occurs because the stratification reduces the  $\langle u'_1 u'_3 \rangle$  correlation and thereby reduces  $P_{13}$ . At low *Re* the remaining mean velocity would quickly be dissipated by viscosity. In the unstratified simulations, 95% of the initial *m.k.e.* is gone within one initial shear period, defined as  $T_S \equiv |\partial \langle u_1 \rangle / \partial r|_{max}^{-1} = 33.3$ . Extrapolating this behaviour to the stratified case, it is expected that if the effect of stratification would not be established within a shear period, the same percentage of *m.k.e.* would be lost to turbulent production. The preservation of *m.k.e.* in the stratified self-propelled wake is thus a phenomenon that should be expected in a regime of high *Re* and low *Fr*.

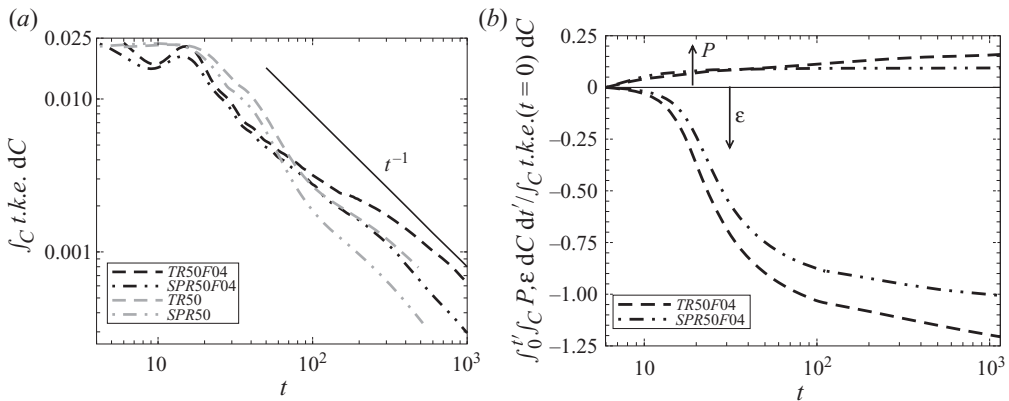


FIGURE 20. (a) Evolution of  $t.k.e.$  (b) Cumulative integrals of production and dissipation normalized by  $t.k.e.0 \equiv \int_C t.k.e.(t=0) dC$ .

This also explains why the effect of stratification that aids the preservation of the wake is stronger in the towed case. The explanation resides in the fact that the initial shear time in the towed case is smaller than in the self-propelled case. Therefore, the towed wake spends a smaller number of shear times in the relatively unstratified near wake region where it transfers less of the  $m.k.e.$  to turbulence before the effects of stratification can disrupt the turbulence production.

### 7.2. Evolution of turbulent kinetic energy

Figure 20(a) shows that the evolution of the  $t.k.e.$  is remarkably similar between the towed (TR50F04) and self-propelled (SPR50F04) cases in the interval  $t_0 < t < 100$  although the  $m.k.e.$  decays much faster in the self-propelled case, (see figure 19a). The turbulent production is ‘not’ the dominant term in the balance of  $t.k.e.$ . Figure 20(b), a plot of the cumulative integrals of  $P$  and  $\epsilon$ , normalized by  $t.k.e.0 \equiv \int_C t.k.e.(t=0) dC$  shows that beyond  $t \approx 30$  the production is insignificant insofar as the  $t.k.e.$  evolution in the self-propelled case. This is consistent with previous studies on unstratified momentumless flows where the shear production of turbulence is dynamically unimportant well before  $t = 100$  (Naudascher 1965; Finson 1975; Higuchi & Kubota 1990; Faure & Robert 1996; Sirvienta & Patel 2000). Figure 20(a) shows that the  $t.k.e.$  is larger in case TR50F04 compared to SPR50F04 after  $t \approx 100$ . This is because the turbulent production, mainly  $P_{12}$ , is larger in the towed case and is also a more significant contributor to the  $t.k.e.$  balance as shown in figure 20(b).

The spatial distribution of the  $t.k.e.$  is shown in figure 21 at  $t = t_0$  and  $t = 1000$ , for the self-propelled cases (figure 21a,c) and towed cases (figure 21b,d). The initial spatial distribution and magnitude of the turbulence, as seen in figures 21(a) and 21(b), is nearly identical between the two cases. At  $t = 1000$ , the towed case shows a more asymmetric profile compared to the self-propelled case. The larger vertical extent in the self-propelled case is partially responsible for the larger  $R_{E3}(t)$  shown in figure 16. At  $t = 1000$  in the towed case (figure 21d) there are two distinct regions of very strong turbulence centred around  $(-4.5, 0)$  and  $(4.5, 0)$ . The large value of the fluctuations in these regions corresponds to the coherent vortex street in the late wake of the towed case. The distinct lobed structure seen in the  $m.k.e.$  of the self-propelled wake, figure 18(a, c, e), is not observed in the  $t.k.e.$

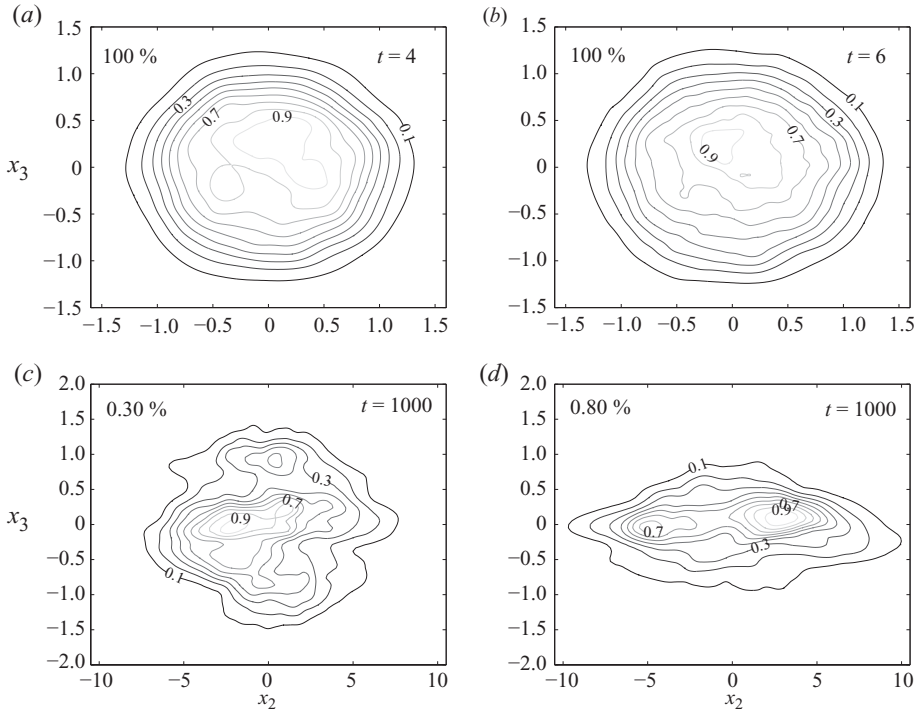


FIGURE 21. Contours of *t.k.e.* Self-Propelled (*a, c*) and towed (*b, d*) at  $t=t_0$  (*a, c*), and  $t=1000$  (*b, d*). The maximum contour level is given in the top left corner as a percentage of the initial maximum *t.k.e.*,  $\approx 0.01$ . The dimensional scale is  $\rho_0 U^2$ .

## 8. Turbulence metrics

### 8.1. Turbulent kinetic energy budget

The area integrated terms in the *t.k.e.* budget are shown in figure 22(*a–d*). The early-time evolution in figure 22(*a*) shows the dissipation rate  $\varepsilon$ , initially much smaller than the production  $P$ , increases owing to nonlinear cascade to fine-scale turbulence and reaches a maximum at  $t \approx 20$ . Later in time,  $30 \lesssim t \lesssim 100$ ,  $\varepsilon$  dominates the other terms as shown in figure 22(*b*), while production becomes small but non-zero in the towed case and negligible in the self-propelled case. As seen in figure 22, the transport of energy by internal waves is the dominant sink of energy between  $100 < t < 300$  in both the towed and self-propelled cases. Subsequently, during  $400 < t < 700$ , there is a strong decrease in the internal wave transport. This time interval exactly corresponds to the duration of the drastic reduction in  $R_{E3}(t)$  seen in figure 16. The period,  $60 < t < 300$ , when the internal wave transport is equal to or greater than the dissipation in figure 22 coincides with the period where the vertical extent  $R_{E3}$  plateaus. This effect is more pronounced in the self-propelled case.

### 8.2. Turbulence components

The directional components, denoted by  $K_{\alpha\alpha} \equiv \langle u'_\alpha u'_\alpha \rangle^{1/2}$  (no summation implied,  $\alpha = 1, 2, 3$ ), of the turbulent velocity field are computed. Figure 23(*a*) shows that the point-wise maximum of turbulence intensity,  $K_{\alpha\alpha}$ , in the horizontal directions ( $\alpha = 2, 3$ ) decreases monotonically for  $t > 15$ . The oscillatory behaviour as well as the growth in the integrated *t.k.e.* (shown earlier in figure 20) at early time is contained almost solely in the vertical component,  $K_{33}$ . This is more evident in figure 23(*b*)

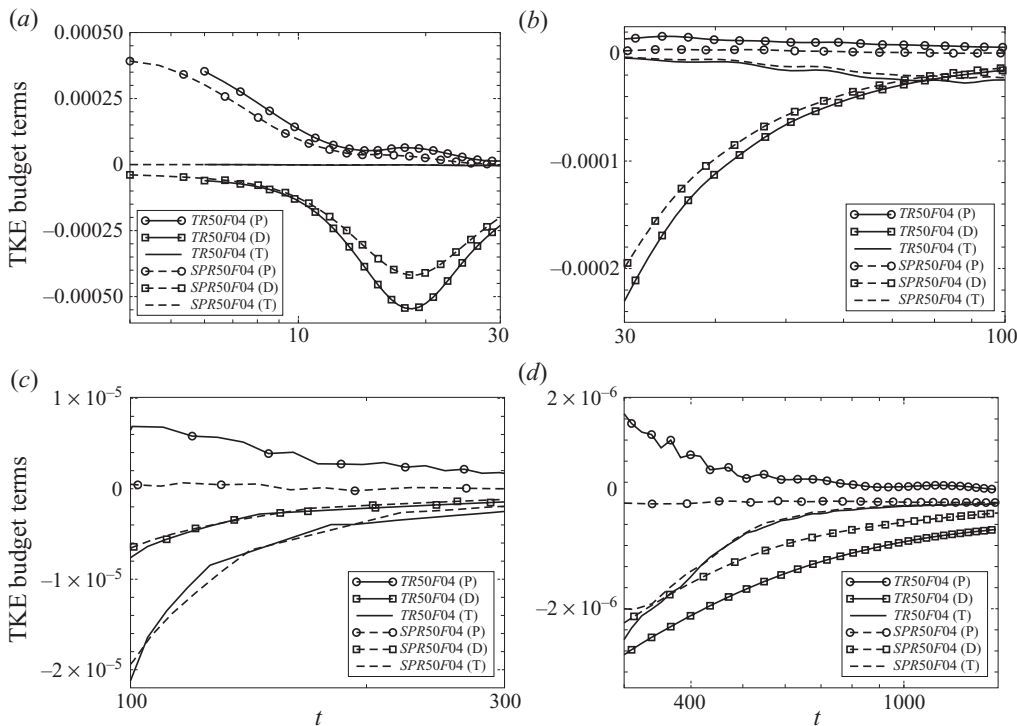


FIGURE 22. Terms in the  $t.k.e.$  budget, (3.5), integrated over the cross-sectional area: (a)  $t_0 < t < 30$ , (b)  $30 < t < 100$ , (c)  $100 < t < 300$  and (d)  $300 < t < 1000$ . Towed curves are in solid lines and self-propelled in dashed. In the figure, (P) stands for production, (D) for dissipation and (T) for transport, as defined in §3.3. The dimensional scale is  $U^3/D$ .

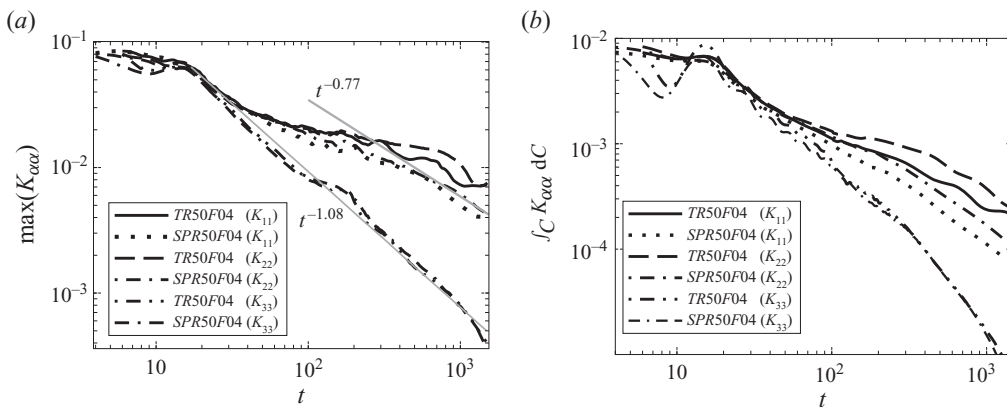


FIGURE 23. Components of root mean square velocity for cases  $TR50F04$  and  $SPR50F04$ : (a) maximum value, (b) integrated value.

which shows the spatially integrated values of the  $t.k.e.$  components.  $K_{33}$  drops nearly 50% and then recovers to nearly its initial value by  $t = 15$ . This is consistent with the large values of the buoyancy flux observed at early time. Both  $K_{11}$  and  $K_{22}$  show a diminished decay rate corresponding to the peak in  $K_{33}$ , indicating that there are some buoyancy effects manifested in the horizontal, although they are nowhere near

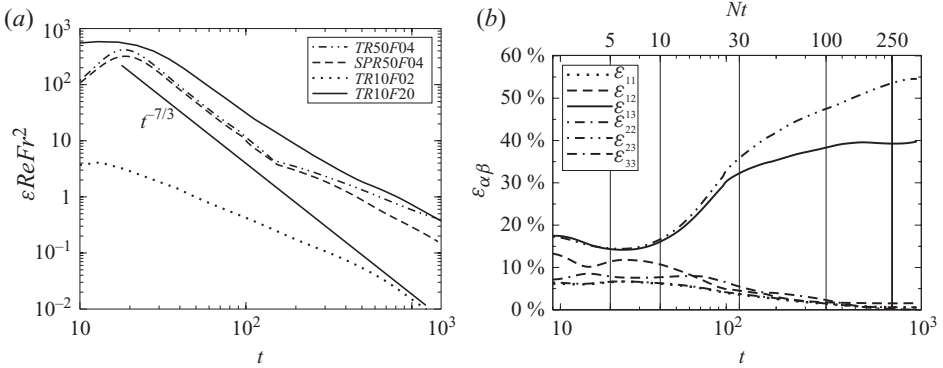


FIGURE 24. (a) Evolution of the non-dimensional turbulent dissipation rate,  $Re_B \equiv \varepsilon^*/(\nu N^{*2}) = \varepsilon Re Fr^2$ . (b) Components of turbulent dissipation rate in the self-propelled case at  $Re = 50\,000$  (*SPR50F04*).

as significant as in the vertical. Interestingly, the horizontal components do not show a decline in regions where  $K_{33}$  decreases, only an increase where  $K_{33}$  also exhibits an increase. The buoyancy flux is larger in the towed case, *TR50F04*, compared to the self-propelled case, *SPR50F04*; this corresponds to not only a more significant recovery of vertical kinetic energy in the near wake but also a slightly larger value of vertical turbulent intensity until  $t = 100$ . The vertical intensity shows an oscillatory modulation which is quite strong initially; however, as shown in figure 23(a), in the late wake  $K_{33}$  scales as  $t^{-1.08}$  similar to the  $t^{-1}$  scaling observed in the experiments of Lin & Pao (1979). The horizontal velocity components in the self-propelled case scale as  $t^{-0.77}$  in agreement with the  $t^{-3/4}$  scaling observed by Lin & Pao (1979). It is worth noting here that the maximum value shown in figure 23(a) can occur far off the wake centreline ( $x_2 = \pm 4.5$ ) at late time in the towed case. This is due to the presence of the coherent vortex street in the late wake in the towed case, which also likely explains why the  $K_{22}$  component is larger than the  $K_{11}$  component. The marked similarity in the evolution of the vertical component between the towed and self-propelled wake simulations reiterate just how effectively stratification has destroyed the mechanism by which turbulence can extract energy from the mean vertical gradients.

### 8.3. Turbulent dissipation rate

The inertial (inviscid) scaling of the turbulent dissipation rate is a cornerstone of high- $Re$  turbulence theory. Inertial scaling,  $\varepsilon^* \sim u^3/l$  where  $u$  is a characteristic fluctuation velocity scale and  $l$  is a large-eddy fluctuation length scale, when combined with the towed wake self-similar scaling laws,  $u \sim t^{-2/3}$  and  $l \sim t^{1/3}$ , gives the following scaling for the dissipation rate in the absence of stratification:  $\varepsilon^* \sim t^{-7/3}$ . The non-dimensional dissipation rate,  $\varepsilon^*/(\nu N^{*2})$ , is considered and calculated as  $\varepsilon Re Fr^2$  since non-dimensionally  $\nu = 1/Re$  and  $N^* = N = 1/Fr$ . Figure 24(a) shows that the non-dimensional dissipation follows a  $t^{-7/3}$  power law in the  $Re = 50\,000$ ,  $Fr = 4$  simulations for a considerable time span. In contrast, there is no evidence of a  $t^{-7/3}$  law for the  $Re = 10\,000$  case at a comparable Froude number,  $Fr = 2$ . The end of the NW region marked by a departure of the mean velocity evolution and mean thickness evolution from unstratified laws occurs much earlier,  $t \simeq 10$ , as discussed previously. Thus, there is a regime of high-Reynolds-number stratified turbulence in the sense that the largest scales of the flow are controlled by buoyancy but the intermediate scales responsible for the nonlinear energy cascade are not, leading

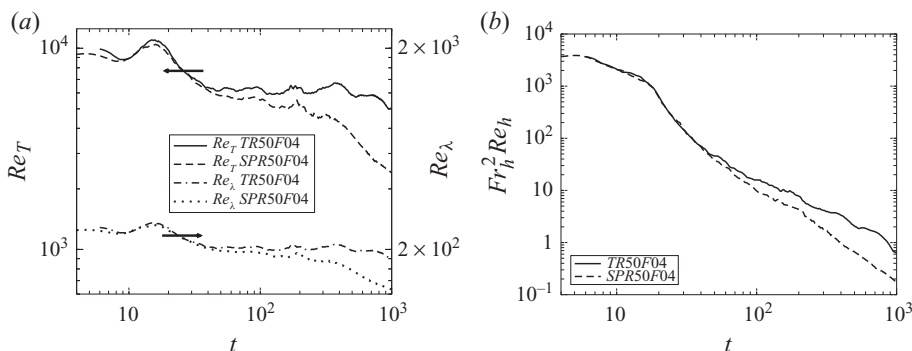


FIGURE 25. (a) Turbulent Reynolds number and Reynolds number based on Taylor microscale. (b) The quantity  $Fr_h^2 Re_h$ .

to a range with inertial scaling. It is worth noting that the  $Re = 10000$  case with high  $Fr = 20$  also shows inertial scaling for some time. At the time when there is departure from inertial scaling, the dissipation rate is such that the non-dimensional quantity,  $\varepsilon^*/\nu N^{*2} = O(1)$ . This can be understood by interpreting  $Re_B \equiv \varepsilon^*/(\nu N^{*2})$  as a buoyancy Reynolds number by choosing the length scale to be the Ozmidov scale,  $(\varepsilon^*/N^{*3})^{1/2}$  and the velocity scale to be  $(\varepsilon^*/N^*)^{1/2}$  in the definition of Reynolds number. Thus, the dissipation rate deviates from  $t^{-7/3}$  scaling when the buoyancy Reynolds number,  $Re_B = O(1)$ .

Figure 24(b) shows the components,  $\varepsilon_{\alpha\beta}$  (Itsweire *et al.* 1993), whose sum equals  $\varepsilon$ . If small-scale isotropy applies,  $\varepsilon_{\alpha\beta} = 2/15$  for  $\alpha \neq \beta$  and  $\varepsilon_{\alpha\beta} = 1/15$  for  $\alpha = \beta$ . There is an approach towards isotropy during the early evolution but, by  $t = 30$ , the two largest components,  $\varepsilon_{13}$  and  $\varepsilon_{23}$ , start becoming more anisotropic. Thus, the tendency towards anisotropy of dissipation rate occurs earlier than the departure of  $\varepsilon$  from inertial scaling. By  $t = 100$  even the smallest components in figure 24(b) start deviating from isotropy. Eventually, in the quasi-two-dimensional stage,  $t > 1000$ , the turbulent dissipation rate is almost entirely due to vertical shear.

The evolution of classically defined Reynolds numbers in figure 25(a) does not shed any light on the observed deviation of  $\varepsilon(t)$  from inertial scaling. The turbulent Reynolds number,  $Re_t = qR_{T2}Re_0$  is defined using the maximum values of  $q(t) = \sqrt{\langle u'_i u'_i \rangle}$  and  $R_{T2}$ , based on (3.6) with  $\langle u_1 \rangle^2$  replaced by  $\langle q \rangle^2$ . The Reynolds number,  $Re_\lambda = \sqrt{20Re_t/3}$ , is based on the Taylor microscale. The initial value of  $Re_t = 10000$  and  $Re_\lambda = 250$  are high, and although, there is a decrease by  $t = 1000$  to  $Re_t = 5000$  and  $Re_\lambda = 183$  in the towed case and  $Re_t = 2500$  and  $Re_\lambda = 130$  in the self-propelled case, the values remain large. Thus, according to measures customary in the turbulence literature, the Reynolds number would be sufficiently large for  $\varepsilon$  to obey inertial scaling throughout the simulation in contradiction to what is actually observed.

Riley & de Bruyn Kops (2003) argue that strongly stratified turbulence can be considered to be high Reynolds number if  $Fr_h^2 Re_h > 1$  because this constraint, with a scaling analysis, can be shown to be equivalent to gradient Richardson number based on fluctuating vertical shear,  $Ri_g < 1$ . Here,  $Fr_h = q_h/R_{T2}Fr$  and  $Re_h = q_h R_{T2} Re_0$  are defined using horizontal length and velocity scales. Figure 25(b) shows that  $Fr_h^2 Re_h \gg 1$  initially. At the time where the inertial scaling of  $\varepsilon$  breaks down,  $Fr_h^2 Re_h = O(1)$ . Recently, Brethouwer *et al.* (2007) concluded from direct simulations of turbulence forced by horizontal motion and a scaling analysis that the parameter  $\mathcal{R} = Re Fr_h^2$  delineated two types of stratified turbulence. In stratified turbulence,  $\mathcal{R} \gg 1$  was a

necessary condition to have a  $k_h^{-5/3}$  power-law of the energy spectrum, small-scale three-dimensional turbulence and increasing isotropy of dissipation rate.

## 9. Conclusions

The evolution of self-propelled and towed wakes in uniformly stratified and unstratified fluids at  $Re = 50\,000$  has been examined using DNS. The present work is the first (to the authors' best knowledge) DNS investigation of self-propelled wakes in archival literature; furthermore, the towed wake simulations extend the Reynolds number of previous DNS studies.

The mean defect velocity and the area-integrated *m.k.e.* in the self-propelled wake decay faster as a function of time than the corresponding towed wake. The decay of area-integrated *m.k.e.* is due to shear production and mean viscous dissipation. The following explanation is advanced to explain the faster decay in the self-propelled cases relative to the corresponding towed cases. For the same peak velocity and wake radius, the mean shear is larger in the self-propelled wake owing to the multi-inflectional profile, and hence the transfer from mean to turbulence by shear production is larger. Buoyancy reduces the Reynolds shear stresses that, in turn, reduces the turbulent production especially that by vertical shear and, therefore, wakes are longer lived in stratified fluids. This buoyancy effect is particularly strong in self-propelled wakes; in an unstratified fluid, turbulent diffusion quickly mixes the mean velocity so that *m.k.e.* reduces to 1% of its initial value by  $t = 100$  while the *m.k.e.* is more than an order of magnitude larger at  $t = 100$  in the corresponding stratified case with the same initial velocity profile. It is worth noting that the effect of Reynolds number is particularly significant in stratified wakes since, once the turbulent production is strongly reduced by buoyancy, the only mechanism by which the remaining *m.k.e.* can be removed is through mean viscous dissipation.

Buoyancy leads to the well-known anisotropy in the velocity distribution of stratified wakes such that the wake spread in the horizontal is much larger than in the vertical. Buoyancy has another important effect in the self-propelled case. The vertical wake structure consisting of lobes of positive and negative velocity are preserved in a stratified fluid owing to a buoyancy induced reduction of vertical turbulent transport and, in particular, the magnitude of the maximum positive velocity at the centreline decays much faster than the magnitude of the minimum negative velocity in the outer lobes. In an unstratified fluid, the outer lobes are rapidly mixed up and not only does the wake velocity profile decay much faster but it also loses its initial shape. The decoupling of layers of positive and negative wake velocity in the vertical that is observed in the present DNS implies that extrapolation of the results of singly inflected profiles (towed wake) to all wake profiles is questionable.

The procedure of Gaussian fits to the mean velocity profile to obtain wake thickness in towed wakes is generalized to more general wake profiles by introducing  $R_i$  based on the central second moment of the squared mean velocity and  $R_{Ei}$  based on the central second moment of the total kinetic energy. Both measures show the vertical thickness of the self-propelled wake is significantly larger than that of the towed wake. Although the mean wake decays faster in the self-propelled case, starting at early time, there is little difference in the evolution of *t.k.e.* during  $t < 100$ . The reason is that the difference in turbulence production between self-propelled and towed cases, important in the *m.k.e.* balance, is less so in the *t.k.e.* balance which becomes quickly dominated by the turbulent dissipation rate. Internal waves are observed in simulations with a stratified fluid. The propagation of momentum away from

the wake by internal waves, although small, fundamentally changes the self-propelled from one with no momentum to one with a small momentum deficit. The wave energy flux is energetically unimportant during the early evolution; however, it becomes the dominant sink of area-integrated *t.k.e.* between  $100 < t < 300$ .

A  $Re = 50\,000$  wake exhibits some differences with respect to that at lower  $Re = 10\,000$ . The NEQ regime is longer at  $Re = 50\,000$  and it includes a distinct phase,  $400 \lesssim t \lesssim 700$ , where the decay rate of mean velocity is significantly reduced, a result that is not apparent at moderate  $Re$  and high  $Fr$ . The NEQ regime in the  $Re = 50\,000$  cases show a time span when the inertial scaling of dissipation rate,  $\varepsilon \sim t^{-7/3}$ , applies as does the  $Re = 10\,000$ ,  $Fr = 20$  case. However, there is no hint of such a power law in the behaviour of  $\varepsilon(t)$  at the lower value of  $Re = 10\,000$ .

Coherent structures in a stratified wake and the evolution of turbulence spectra are also of interest. These topics will be addressed in a follow-up study.

We would like to acknowledge Dr Ron Joslin with the United States Office of Naval Research for the support through ONR grant N00014-07-10133. We are grateful to Dr Doug Dommermuth at Science Applications International Corporation for providing the supercomputing time required for the large DNS runs. The authors would like to acknowledge and thank the reviewers for their constructive and helpful reviews. This work was supported in part by a grant of computer time from the DOD High Performance Computing Modernization Program (<http://www.hpcmo.hpc.mil/>). The numerical simulations have been performed on the Cray XT4 at the US Army Corps of Engineers Engineering Research and Development Center.

## REFERENCES

- BASAK, S. 2005 Dynamics of stratified shear layers with horizontal shear. PhD thesis, University of California, San Diego, CA.
- BASAK, S. & SARKAR, S. 2006 Dynamics of a stratified shear layer with horizontal shear. *J. Fluid Mech.* **568**, 19–54.
- BEVILAQUA, P. M. & LYKOUKDIS, P. S. 1978 Turbulence memory in self-preserving wakes. *J. Fluid Mech.* **89** (3), 589–606.
- BONNIER, M., BONNETON, P. & EIFF, O. 1998 Far-wake of a sphere in a stably stratified fluid: characterization of the vortex structures. *Appl. Sci. Res.* **59**, 269–281.
- BONNIER, M. & EIFF, O. 2002 Experimental investigation of the collapse of a turbulent wake in a stably stratified fluid. *Phys. Fluids* **14** (2), 791–801.
- BRETHOUWER, G., BILLANT, P., LINDBORG, E. & CHOMAZ, J.-M. 2007 Scaling analysis and simulation of strongly stratified turbulent flow. *J. Fluid Mech.* **585**, 343–368.
- BRUCKER, K. A. & SARKAR, S. 2007 Evolution of an initially turbulent stratified shear flow. *Phys. Fluids* **19** (10), 105105.
- CHOMAZ, J.-M., BONNETON, P. & HOPFINGER, E. J. 1993 The structure of the near wake of a sphere moving horizontally in a stratified fluid. *J. Fluid Mech.* **254**, 1–21.
- DIAMESSIS, P. J., DOMARADZKI, J. A. & HESTHAVEN, J. S. 2005 A spectral multidomain penalty method model for the simulation of high Reynolds number localized incompressible stratified turbulence. *J. Comput. Phys.* **202** (1), 298–322.
- DIAMESSIS, P. J. & SPEDDING, G. R. 2006 Scaling and structure of turbulent wakes at high Reynolds number. *Proceedings of the Sixth International Symposium on Stratified Flows*, 11–14 December, 2006, Perth, Australia.
- DOMMERMUTH, D., ROTTMAN, J. W., INNIS, G. E. & NOVIKOV, E. A. 2002 Numerical simulation of the wake of a towed sphere in a weakly stratified fluid. *J. Fluid Mech.* **473**, 83–101.
- FAURE, T. & ROBERT, G. 1996 Turbulent kinetic energy balance in the wake of a self-propelled body. *Exp. Fluids* **21** (4), 268–274.
- FINSON, M. L. 1975 Similarity behaviour of momentumless turbulent wakes. *J. Fluid Mech.* **71** (3), 465–479.

- GHOSAL, S. & ROGERS, M. M. 1997 A numerical study of self-similarity in a turbulent plane wake using large-eddy simulation. *Phys. Fluids* **9** (6), 1729–1739.
- GOURLAY, M. J., ARENDT, S. C., FRITTS, D. C. & WERNE, J. 2001 Numerical modelling of initially turbulent wakes with net momentum. *Phys. Fluids* **13** (12), 3783–3802.
- GRAN, R. L. 1973 An Experiment on the wake of a propeller driven body. *Tech. Rep. Rept.* 20086-6006-RU-00. TRW Systems, Redondo Beach, CA.
- HIGUCHI, H. & KUBOTA, T. 1990 Axisymmetric wakes behind a slender body including zero-momentum configurations. *Phys. Fluids A* **2** (9), 1615–1623.
- ITSWEIRE, E. C., KOSEFF, J. R., BRIGGS, D. A. & FERZIGER, J. H. 1993 Turbulence in stratified shear flows: implications for interpreting shear-induced mixing in the ocean. *J. Phys. Oceanogr.* **23** (7), 1508–1522.
- LIN, Q., BOYER, D. L. & FERNANDO, H. J. S. 1992 Turbulent wakes of linearly stratified flow past a sphere. *Phys. Fluids A* **4** (8), 1687–1696.
- LIN, J.-T. & PAO, Y.-H. 1974 The turbulent wake of a propeller-driven slender body in a stratified fluid. *Tech. Rep.* 14. Flow Research Inc.
- LIN, J.-T. & PAO, Y.-H. 1979 Wakes in stratified fluids. *Annu. Rev. Fluid Mech.* **11**, 317–338.
- LOFQUIST, K. E. B. & PURTELL, P. 1984 Drag on a sphere moving horizontally through a stratified liquid. *J. Fluid Mech.* **148**, 271–284.
- MEUNIER, P. & SPEDDING, G. R. 2006 Stratified propelled wakes. *J. Fluid Mech.* **552**, 229–256.
- MOSER, R. D., ROGERS, M. M. & EWING, D. W. 1998 Self-similarity of time-evolving plane wakes. *J. Fluid Mech.* **367**, 255–289.
- NAUDASCHER, E. 1965 Flow in the wake of self-propelled bodies and related sources of turbulence. *J. Fluid Mech.* **22** (4), 625–656.
- PHAM, H., SARKAR, S. & BRUCKER, K. A. 2009 Dynamics of a stratified shear layer above a region of deep stratification. *J. Fluid Mech.* **630**, 191–223.
- RILEY, J. J. & DE BRUYN KOPS, S. M. 2003 Dynamics of turbulence strongly influenced by buoyancy. *Phys. Fluids* **15** (7), 2047–2059.
- ROGALLO, R. S. 1981 Numerical experiments in homogeneous turbulence. *Tech. Rep.* TM-81315. NASA, Ames Research Center.
- ROGERS, M. M. & MOSER, R. D. 1994 Direct simulation of a self-similar turbulent mixing layer. *Phys. Fluids* **6** (2), 903–923.
- ROTTMAN, J. W., DOMMERMUTH, D. G., INNIS, G. E., O'SHEA, T. T. & NOVIKOV, E. 2003 Numerical simulation of wakes in a weakly stratified fluid. *Proceedings of the 24th Symposium on Naval Hydrodynamics*, 8–13 July, 2002, Fukuoka, Japan, pp. 517–533.
- SIRVIENTE, A. I. & PATEL, V. C. 2000 Wake of a self-propelled body. Part 1. Momentumless wake. *AIAA J.* **38** (4), 613–619.
- SPEDDING, G. R. 1997 The evolution of initially-turbulent bluff body wakes of at high internal froude number. *J. Fluid Mech.* **337**, 283–301.
- SPEDDING, G. R. 2001 Anisotropy in turbulence profiles of stratified wakes. *Phys. Fluids* **13** (8), 2361–2372.
- SPEDDING, G. R. 2002 Vertical structure in stratified wakes with high initial froude number. *J. Fluid Mech.* **454**, 71–112.
- SPEDDING, G. R., BROWAND, F. K. & FINCHAM, A. M. 1996 The long-time evolution of the initially turbulent wake of a sphere in a stable stratification. *Dyn. Atmos. Oceans* **23** (1–4), 171–182.
- TENNEKES, H. & LUMLEY, J. L. 1972 *A First Course in Turbulence*. The MIT Press.
- UBEROI, M. S. & FREYMUTH, P. 1970 Turbulent energy balance and spectra of the axisymmetric wake. *Phys. Fluids* **13** (9), 2205–2210.
- VOROPAYEV, S. I. & FERNANDO, H. J. S. 2009 Wakes of maneuvering body in stratified fluid. In *Proceedings of the European Consortium for Mathematics in Industry (ECMI) 2008 Conference*, 30 June–4 July, 2008, London.
- VOROPAYEV, S. I., MCEACHERN, G. B., FERNANDO, H. J. S. & BOYER, D. L. 1999 Large vortex structures behind a maneuvering body in stratified fluids. *Phys. Fluids* **11** (6), 1682–1684.
- WILLIAMSON, J. H. 1980 Low-storage Runge–Kutta schemes. *J. Comput. Phys.* **35**, 48–56.